Study on Gas/Liquid Pulsed Discharge Plasma in a Slug Flow Reactor for Nanoparticles Synthesis and Dye Decomposition

A Doctoral Dissertation by

ZHU Wanying

2022

Graduate School of Engineering,

Department of Materials Process Engineering,

Nagoya University

List of contents

Chapter 1. General Introduction

1.1 Plasma

Plasma is often referred to be the fourth state of matter, which is obtained by increasing the energy level from a solid state through the liquid and gaseous state of matter, ending in an ionized state of gas[1]. The relationship between plasma and three states of matter is shown in Figure 1.1. Matter consists of a large number of molecules, which can be further divided into atoms. According to the nuclear structure model of the atom[2], there is a positive nucleus inside the atom, and negative electrons outside the nucleus. When supplying enough energy to the atoms of a neutral gas, the outside electrons obtain higher energy and might escape from the electric field force of the nucleus, becoming independent free electrons[3]. Hence, matter changes into a homogeneous ionized state consisting of positive and negative species[4], appearing as an electrified gas[5]. Because the total positive and negative species are equal, plasma is electrically neutral.

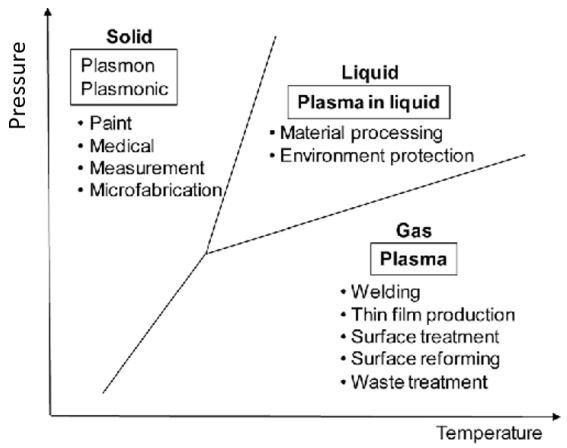

Figure 1.1 Relationship between plasma and the three states of matter[6]

During the reactions on plasma, electrons are accelerated in the local electric field and collide with the neutral molecules and atoms in the feed gas, producing electrons and ions[7]. According to the electron temperature T_e and ion temperature T_i, plasma can be distinguished into thermal plasmas and non-thermal plasma[5]. Figure 1.2 shows the typical ranges of temperatures and electron densities for thermal and non-thermal plasmas[8]. Thermal plasmas are characterized by the relatively high electron densities and the low T_e, and T_e is basically equal to T_i ($T_e \approx T_i$), indicating local thermodynamic equilibrium. Thermal plasmas are commonly generated by plasma torches, and microwave devices, producing a high flux of heat[9]. And they are mainly used in waste treatment[10] and plasma material processing[8]. In contrast, non-thermal plasmas are characterized by their relatively low electron densities and high T_e. And T_e is much higher than T_i ($T_e >> T_i$), originating from that most of the coupled electrical energy is mainly channeled to the electron to produce energetic electrons.

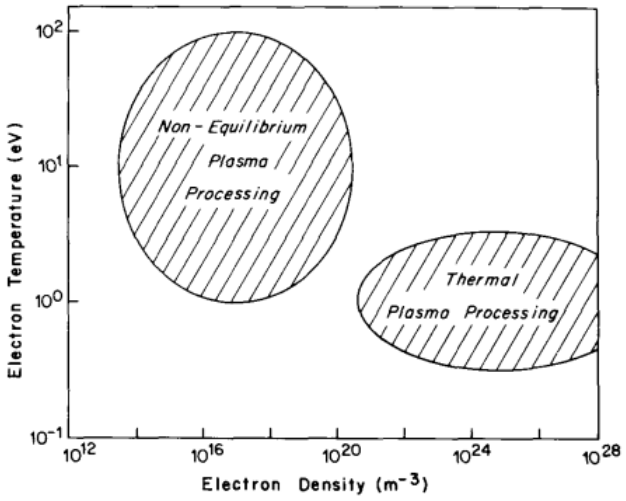

Figure 1.2 Typical ranges of temperatures and electron densities for thermal and non-thermal plasmas[8]

1.2 Cold plasma technology

Non-thermal plasmas, also known as cold plasmas, are novel technologies[11] and are applied in various applications, including food industry[12], dye treatment[13], degradation of pharmaceutical compounds[14-15], surface modification[16], functionalization of polymers[17], and methane conversion[18]. Dasan et al.[19] reported the process for decontamination of food contact surfaces using cold plasma, showing the advantages of low temperature, minimal nutrient destruction, and absence of toxic by-products. Sarangpapani et al.[20] reported the effective chemical dissipation of agrochemicals on blueberries using atmospheric cold plasma, retaining nutritional quality parameters. Yavuz et al.[21] reported the process of surface modification on kaolin using cold plasma, with clean reaction, short processing time, less energy consumption, and a small fiber damage[22]. Cold plasma enables many generic surface modification processes, including surface activation by breaking bond to create reactive sites, grafting of functional groups and chemical moieties, volatilization and etching of materials, dissociation if surface contaminants and deposition of conformal coating[23]. During the plasma treatments, gases are applied into the materials surface to generate chemical functionalities, such as –OH, –CO, –COOH[24], binding other molecules or polymers to the surface to achieve specific chemical properties[25]. Wen et al.[26] reported the process of chitosan treatment using glow discharge plasma, increasing the number of $–CH_2$ and $–CH_3$ groups and enhancing the ability for dye removal.

1.3 Discharge plasma generated in a gas/liquid environment

1.3.1 Gas/liquid pulsed discharge plasma

For a gas/liquid environment, plasma is generated in the gas phase and the major reaction proceeds in the liquid phase. Discharge plasma is usually easier to generate in a gas medium than in a liquid medium[27]. Hence, lower energy and operating cost are required to produce plasma in a gas/liquid environment than as a direct discharge in a liquid[28]. Furthermore, the gas-liquid interface surface area is large, making it highly effective for gaseous species to diffuse inside the liquid[29]. When high-energy electrons are introduced into a gas/liquid environment, gas molecules or atoms are ionized first to form initial radicals. Then, the generated radicals make contact and react with molecules in the liquid medium via the gas/liquid interface, leading to the generation of various radical species with high reactivity in the liquid phase, including hydrogen radicals (H·), hydroxyl radicals (OH·), oxygen (O_2), hydrogen peroxide (H_2O_2), and ozone (O_3) species [30-32]. Rong et al.[33] reported that OH· radicals play a key role in the degradation of pharmaceutical compounds by plasma. Rahimpour et al.[34] found that plasma produces O_3 and other oxidants, which are very useful in the decomposition of organic pollutants in industrial wastewater. In addition, toxic reagents and ligands are not required in the plasma system, being an environmentally friendly process. And it was feasible to operate at room temperature, reducing the operating cost. Based on the above advantages, gas/liquid discharge plasma has been applied in various fields, including dye treatment[35-36], degradation of pharmaceutical compounds[37-38], and synthesis of nanomaterials[39].

Common methods to produce plasma in gas/liquid environments are to locate the

electrode above the liquid surface, or to immerse the electrode in the liquid[40-41]. The metal/metal ions vaporized from the electrode can be introduced into the liquid phase, leading to the contamination of the system. In conventional gas/liquid interface plasma reactions, gas is introduced from the bottom of a tank reactor and floated due to buoyancy, and plasma is generated inside the bubbles[42-43]. This method significantly increases the interface between the gas and liquid media. But the bubbles deform, coalesce to become larger, break up to become smaller, or move erratically providing a very non-uniform plasma reaction field. In addition, the treatment capacity is also limited by the tank reactor.

1.3.2 Slug flow system using pulsed discharge plasma

In order to solve the above problem, we developed a slug flow plasma system that provides a very uniform plasma reaction field as the bubbles are not deformed and move regularly[13]. The slug flow plasma reaction method consisted of a continuous alternating flow of gas and feed solution through a capillary glass tube with copper electrodes on the outside. Stable plasma was produced when the bubbles flowed through the electrodes at a high voltage. The shapes and sizes of the bubbles were uniform. The circulating flow in the liquid induced by the friction at the solid surface also accelerated the uniform reaction[44], as shown in Figure 1.3. It was possible to maintain a uniform interface with a high specific surface area in the system. Therefore, the slug flow system provides an easy, continuous, and environmentally friendly process and has been applied successfully to the decomposition of methyl blue[45], and synthesis of silver

nanoparticles[46].

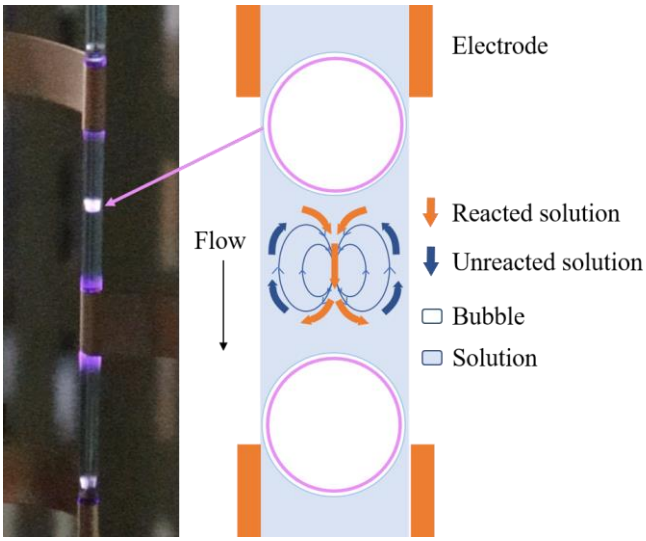

Figure 1.3 Generation of plasma in gas/liquid interface and continuous circulating convective flow in slug flow system

1.4 Previous work

1.4.1 Experimental methods

In our previous study, a slug flow system using atmospheric-pressure pulsed discharge plasma has been proposed[45]. The apparatus scheme is shown in the Figure 1.4. Gas and liquid were introduced into the system by a gas valve and a solution pump, generating the bubbles and continuous gas-liquid interfaces. And the flow rates of gas and liquid were set at 0.15 mL/min and 1.5 mL/min, respectively. Copper sheets were placed outside the capillary glass tube with an interval of 25 mm, connecting to an alternating current (AC) pulse power supply and ground as high-voltage electrode and ground electrode, respectively. The AC pulse power supply was used as a frequency of

10 kHz. The voltage and current waveforms are shown in Figure 1.5. Sodium chloride was added into the feed solution for plasma generation, providing a conductivity of 500 μS/cm. Argon, helium, oxygen, and nitrogen were used as input gas, respectively.

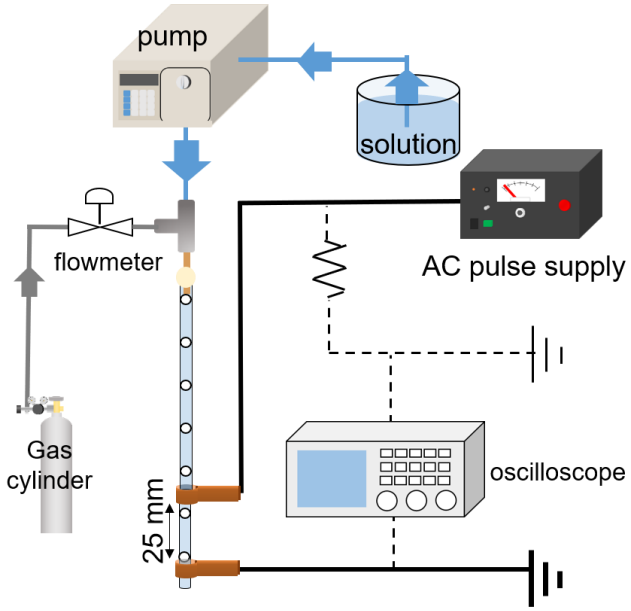

Figure 1.4 Apparatus scheme of pulsed discharge plasma generation in a slug flow system under atmospheric-pressure condition[45]

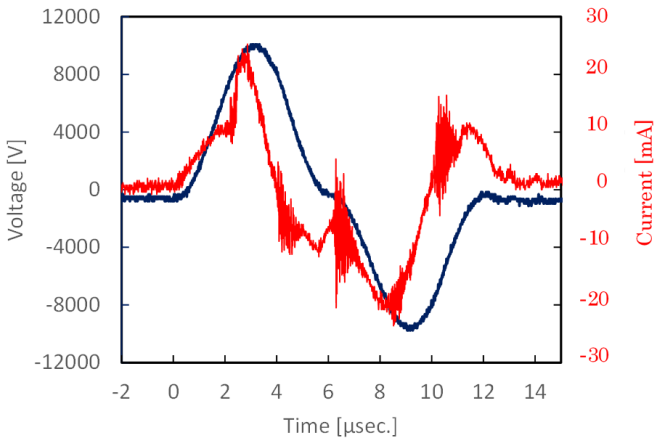

Figure 1.5 The voltage and current waveforms of AC power supply[45]

1.4.2 Analysis of discharge plasma in the slug flow system

Figure 1.6 shows the images of pulsed discharge plasma on the gas/liquid surface of bubbles in the slug flow system during 7 msec, captured using a high -speed camera. Figure 1.7 shows the emission intensity at the gas/liquid surface when the pulsed discharge plasma is applied, captured using a charge-coupled device (CCD) camera. Joshi et al.[47] found that propagation of discharge plasma can be detected by a camera device due to its different optical refractive index from surrounding liquid. Hence, the interaction of pulsed discharge plasma on gas-liquid bubble motion can be observed visually. It can also be observed that the surface of the bubble is disturbed by winkles, originating from the filamentary discharge scheme along the inner surface of the bubble[43]. It indicates the electrical field distribution on the surface of gas-liquid bubble after applying the pulsed discharge plasma. After high voltage is introduced, the pulsed discharge plasma may generate immediately and propagate toward the gas-liquid surface. A certain current is also found during the propagation process, attributing to the moving charged species. But it seems not uniform for the electrical field distribution on the gas-liquid surface, indicating that electrical field on the gas-liquid surface near the capillary glass wall is higher than that on the axis[45]. Tachibana et al.[43] also found a similar result, attributing to the surface charges accumulated on the interface of the bubble and Maxwell tensor-type force.

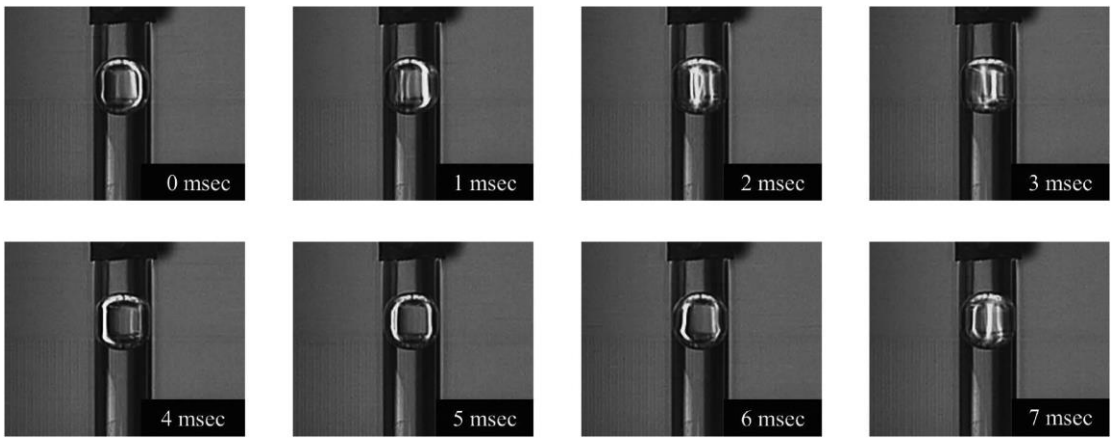

Figure 1.6 Images of pulsed discharge plasma in a slug flow system[45]

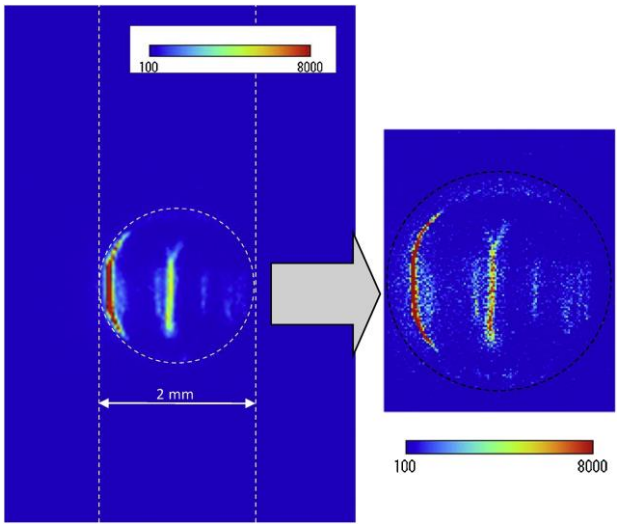

Figure 1.7 Typical pulsed discharge plasma image on the surface of a bubble in the slug flow system with argon as gas phase[45]

1.4.3 Effect of experimental factors on plasma generation

1.4.3.1 Gas-liquid ratio

The relationship between gas-liquid ration and initiation discharge voltage was investigated. The flow rate of feed solution was kept constant at 1.5 mL/min, and the

distances of adjacent bubbles were set by adjusting the flow rate of gas at 11, 13, and 15 mm, respectively. The gas-liquid ratio and the corresponding initiation discharge voltage are shown in the Table 1.1. Even a voltage of 13 kV was applied into the system, discharge plasma cannot be generated when the distance was set at 9 mm. As the number of bubbles between the electrodes increased, the electrical resistance of gas phase increased, resulting in an increase on difficulty to break down the gas and produce plasma. Hence, required initiation discharge voltage also increased.

Table 1.1 The relationship between different liquid-gas ratio and initiation discharge voltage

Distance of adjacent bubbles/ mm	Liquid-gas ratio	Initiation discharge voltage/ kV
11	6.6	9.5
13	7.8	8.7
15	9.0	7.5

1.4.3.2 Conductivity of feed solution

The relationship between conductivity of feed solution and initiation discharge voltage was investigated. Conductivity was adjusted by adding sodium chloride into the feed solution, and result is shown in Figure 1.8. It is difficult to produce discharge plasma when the conductivity is too low, even if applied voltage continues to be increased. Discharge plasma cannot be produced with conductivity less than 100 μS/cm even if a voltage of 14 kV is applied. With the conductivity of feed solution increasing,

it became easier to break down the gas, resulting in decreasing required initiation voltage.

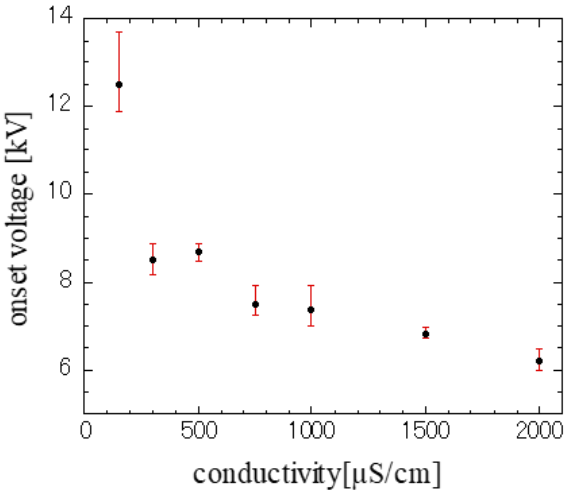

Figure 1.8 The relationship between conductivity of feed solution and initiation discharge voltage

1.4.3.3 Gas sources

The relationship between gas sources and initiation discharge voltage was investigated. Argon (Ar), helium (He), oxygen (O_2), and nitrogen (N_2) were used as feed gas, respectively. The corresponding initiation discharge voltages are shown in Figure 1.9. Results shown that it was more difficult to cause dielectric breakdown when using O_2 and N_2 as feed gas, resulting in the higher voltages. When monatomic Ar and He were used as feed gas, discharge plasma tended to be generated easily.

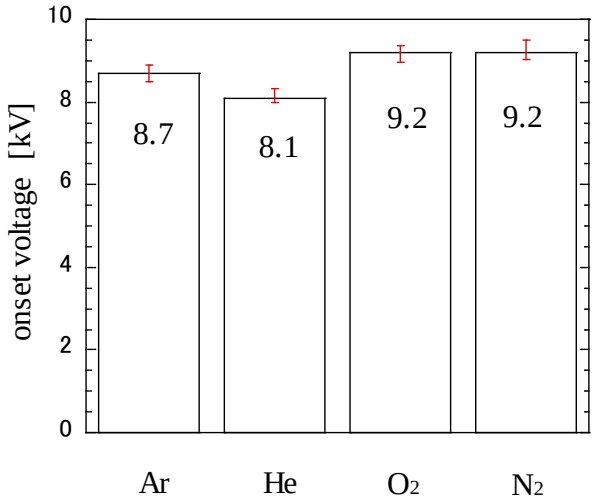

Figure 1.9 The relationship between gas sources and initiation discharge voltage

1.5 Motivation and purpose of this work

This work is mainly based on the slug flow system proposed in our previous study. Compared with traditional methods to produce plasma in a gas/liquid environment, the slug flow system provides a uniform and continuous reaction field. Hence, the system is to be applied into various reaction processes to create new applications and to examine its advantages. In this study, this system is to be applied on the synthesis of metal oxide nanoparticles. Reaction mechanism and effect of experimental factors are to be studied. And this system is first to be implemented under pressurized conditions. Chemical properties of the system under pressurized conditions are to be observed, and the effect of pressure on the system is to be investigated.

References

1. Hojnik, N.; Cvelbar, U.; Tavcar-Kalcher, G.; Walsh, J.; Križaj, I., Mycotoxin Decontamination of Food: Cold Atmospheric Pressure Plasma versus "Classic" Decontamination. *Toxins* **2017,** *9*, 151.
2. Hodgson, P. E., *Nuclear reactions and nuclear structure*. Clarendon Press Oxford: 1971; Vol. 426.
3. Brown, S. C., Basic data of plasma physics: The fundamental data on electrical discharges in gases. MIT Press. **1966**.
4. Lieberman, M. A.; Lichtenberg, A. J., *Principles of plasma discharges and materials processing*. John Wiley & Sons: 2005.
5. Nehra, V.; Kumar, A.; Dwivedi, H., Atmospheric non-thermal plasma sources. *International Journal of Engineering* **2008,** *2* (1), 53-68.
6. Horikoshi, S.; Serpone, N., In-liquid plasma: a novel tool in the fabrication of nanomaterials and in the treatment of wastewaters. *RSC Advances* **2017,** *7*, 47196-47218.
7. Conrads, H.; Schmidt, M., Plasma generation and plasma sources. *Plasma Sources Science and Technology* **2000,** *9* (4), 441.
8. Boulos, M. I., Thermal plasma processing. *IEEE transactions on Plasma Science* **1991,** *19* (6), 1078-1089.
9. Gleizes, A.; Gonzalez, J.-J.; Freton, P., Thermal plasma modelling. *Journal of Physics D: Applied Physics* **2005,** *38* (9), R153.
10. Gomez, E.; Rani, D. A.; Cheeseman, C.; Deegan, D.; Wise, M.; Boccaccini, A., Thermal plasma technology for the treatment of wastes: A critical review. *Journal of hazardous materials* **2009,** *161* (2-3), 614-626.
11. Lu, X.; Yan, P.; Ren, C.; Shao, T., Review on atmospheric pressure pulsed DC discharge. *SCIENTIA SINICA Physica, Mechanica & Astronomica* **2011,** *41* (7), 801-815.
12. Chizoba Ekezie, F.-G.; Sun, D.-W.; Cheng, J.-H., A review on recent advances in cold plasma technology for the food industry: Current applications and future trends. *Trends in Food Science & Technology* **2017,** *69*, 46-58.
13. Yamada, M.; Machmudah, S.; Kanda, H.; Goto, M., Nonthermal Atmospheric Pressure Plasma for Methylene Blue Dye Decolorization by Using Slug Flow Reactor System. *Plasma Chemistry and Plasma Processing* **2020**, 1-16.
14. Guo, H.; Li, Z.; Zhang, Y.; Jiang, N.; Wang, H.; Li, J., Degradation of chloramphenicol by pulsed discharge plasma with heterogeneous Fenton process using Fe3O4 nanocomposites. *Separation and Purification Technology* **2020,** *253*, 117540.
15. Guo, H.; Jiang, N.; Wang, H.; Shang, K.; Lu, N.; Li, J.; Wu, Y., Enhanced catalytic performance of graphene-TiO2 nanocomposites for synergetic degradation of fluoroquinolone antibiotic in pulsed discharge plasma system. *Applied Catalysis B: Environmental* **2019,** *248*, 552-566.
16. Shao, T.; Zhang, C.; Long, K.; Zhang, D.; Wang, J.; Yan, P.; Zhou, Y., Surface modification of polyimide films using unipolar nanosecond-pulse DBD in atmospheric air. *Applied Surface Science* **2010,** *256* (12), 3888-3894.

17. Pankaj, S. K.; Keener, K. M., Cold plasma: background, applications and current trends. *Current Opinion in Food Science* **2017,** *16*, 49-52.
18. Tu, X.; Gallon, H. J.; Twigg, M. V.; Gorry, P. A.; Whitehead, J. C., Dry reforming of methane over a Ni/Al2O3 catalyst in a coaxial dielectric barrier discharge reactor. *Journal of Physics D: Applied Physics* **2011,** *44* (27), 274007.
19. Dasan, B. G.; Onal-Ulusoy, B.; Pawlat, J.; Diatczyk, J.; Sen, Y.; Mutlu, M., A new and simple approach for decontamination of food contact surfaces with gliding arc discharge atmospheric non-thermal plasma. *Food and Bioprocess Technology* **2017,** *10* (4), 650-661.
20. Sarangapani, C.; O'Toole, G.; Cullen, P.; Bourke, P., Atmospheric cold plasma dissipation efficiency of agrochemicals on blueberries. *Innovative Food Science & Emerging Technologies* **2017,** *44*, 235-241.
21. Yavuz, Ö.; Saka, C., Surface modification with cold plasma application on kaolin and its effects on the adsorption of methylene blue. *Applied Clay Science* **2013,** *85*, 96-102.
22. Ren, C.-S.; Wang, K.; Nie, Q.-Y.; Wang, D.-Z.; Guo, S.-H., Surface modification of PE film by DBD plasma in air. *Applied surface science* **2008,** *255* (5), 3421-3425.
23. Chan, C. M., Polymer surface modification and characterization. Hanser Pub Inc. 1993.
24. Shen, W.; Li, Z.; Liu, Y., Surface chemical functional groups modification of porous carbon. *Recent Patents on Chemical Engineering* **2008,** *1* (1), 27-40.
25. Desmet, T.; Morent, R.; De Geyter, N.; Leys, C.; Schacht, E.; Dubruel, P., Nonthermal plasma technology as a versatile strategy for polymeric biomaterials surface modification: a review. *Biomacromolecules* **2009,** *10* (9), 2351-2378.
26. Wen, Y.; Shen, C.; Ni, Y.; Tong, S.; Yu, F., Glow discharge plasma in water: a green approach to enhancing ability of chitosan for dye removal. *Journal of hazardous materials* **2012,** *201*, 162-169.
27. Nijdam, S.; van Veldhuizen, E.; Bruggeman, P.; Ebert, U., An Introduction to Nonequilibrium Plasmas at Atmospheric Pressure. In *Plasma Chemistry and Catalysis in Gases and Liquids*, pp 1-44.
28. Diono, W.; Machmudah, S.; Kanda, H.; Zhao, Y.; Goto, M., Pulsed Discharge Plasma in High-Pressure Environment for Water Pollutant Degradation and Nanoparticle Synthesis. *Plasma* **2021,** *4* (2), 309-331.
29. Zeghioud, H.; Nguyen-Tri, P.; Khezami, L.; Amrane, A.; Assadi, A. A., Review on discharge Plasma for water treatment: mechanism, reactor geometries, active species and combined processes. *Journal of Water Process Engineering* **2020,** *38*, 101664.
30. Cao, Y.; Qu, G.; Li, T.; Jiang, N.; Wang, T., Review on reactive species in water treatment using electrical discharge plasma: formation, measurement, mechanisms and mass transfer. *Plasma Science and Technology* **2018,** *20* (10), 103001.
31. Kanazawa, S.; Kawano, H.; Watanabe, S.; Furuki, T.; Akamine, S.; Ichiki, R.; Ohkubo, T.; Kocik, M.; Mizeraczyk, J., Observation of OH radicals produced by pulsed discharges on the surface of a liquid. *Plasma Sources Science and Technology* **2011,** *20* (3), 034010.
32. Marotta, E.; Schiorlin, M.; Ren, X.; Rea, M.; Paradisi, C., Advanced oxidation

process for degradation of aqueous phenol in a dielectric barrier discharge reactor. *Plasma Processes and Polymers* **2011,** *8* (9), 867-875.
33. Rong, S.-P.; Sun, Y.-B.; Zhao, Z.-H., Degradation of sulfadiazine antibiotics by water falling film dielectric barrier discharge. *Chinese Chemical Letters* **2014,** *25* (1), 187-192.
34. Rahimpour, M.; Taghvaei, H.; Zafarnak, S.; Rahimpour, M. R.; Raeissi, S., Post-discharge DBD plasma treatment for degradation of organic dye in water: A comparison with different plasma operation methods. *Journal of Environmental Chemical Engineering* **2019,** *7* (4), 103220.
35. Xin, Y.-Y.; Zhou, L.; Ma, K.-k.; Lee, J.; Qazi, H.; Li, H.-P.; Bao, C.-Y.; Zhou, Y.-X., Removal of bromoamine acid in dye wastewater by gas-liquid plasma: The role of ozone and hydroxyl radical. *Journal of Water Process Engineering* **2020,** *37*, 101457.
36. Nau-Hix, C.; Holsen, T. M.; Thagard, S. M., Influence of solution electrical conductivity and ionic composition on the performance of a gas–liquid pulsed spark discharge reactor for water treatment. *Journal of Applied Physics* **2021,** *130* (12), 123301.
37. Corella Puertas, E.; Peyot, M.-L.; Pineda, M.; Volk, K.; Coulombe, S.; Yargeau, V., Degradation of diatrizoate in a pin-to-liquid plasma reactor, its transformation products and their residual toxicity. *Science of The Total Environment* **2021,** *782*, 146895.
38. Wang, X.; Luo, J.; Huang, Y.; Mei, J.; Chen, Y., Degradation of pharmaceutical contaminants by bubbling gas phase surface discharge plasma combined with gC 3 N 4 photocatalysis. *Environmental Science: Water Research & Technology* **2021,** *7* (3), 610-621.
39. Nguyen, L. N.; Lamichhane, P.; Choi, E. H.; Lee, G. J., Structural and Optical Sensing Properties of Nonthermal Atmospheric Plasma-Synthesized Polyethylene Glycol-Functionalized Gold Nanoparticles. *Nanomaterials* **2021,** *11* (7), 1678.
40. Lin, L.; Ma, X.; Li, S.; Wouters, M.; Hessel, V., Plasma-electrochemical synthesis of europium doped cerium oxide nanoparticles. *Frontiers of Chemical Science and Engineering* **2019,** *13* (3), 501-510.
41. Shen, J.; Zhang, H.; Xu, Z.; Zhang, Z.; Cheng, C.; Ni, G.; Lan, Y.; Meng, Y.; Xia, W.; Chu, P. K., Preferential production of reactive species and bactericidal efficacy of gas-liquid plasma discharge. *Chemical Engineering Journal* **2019,** *362*, 402-412.
42. Sato, K.; Yasuoka, K., Pulsed Discharge Development in Oxygen, Argon, and Helium Bubbles in Water. *IEEE Transactions on Plasma Science* **2008,** *36* (4), 1144-1145.
43. Tachibana, K.; Takekata, Y.; Mizumoto, Y.; Motomura, H.; Jinno, M., Analysis of a pulsed discharge within single bubbles in water under synchronized conditions. *Plasma Sources Science and Technology* **2011,** *20* (3), 034005.
44. Diono, W.; Mano, K.; Hayashi, Y.; Yamada, M.; Takahashi, S.; Takada, N.; Kanda, H.; Goto, M., Atmospheric-pressure pulsed discharge plasma in capillary slug flow system for dye decomposition. *Chemical Engineering and Processing - Process Intensification* **2018,** *135*.
45. Mano, K.; Hayashi, Y.; Yamada, M.; Takahashi, S.; Takada, N.; Kanda, H.; Goto, M., Atmospheric-pressure pulsed discharge plasma in capillary slug flow system for

dye decomposition. *Chemical Engineering and Processing-Process Intensification* **2019,** *135*, 133-140.
46. Yamada, M.; Takahashi, S.; Wahyudiono; Takada, N.; Kanda, H.; Goto, M., Synthesis of silver nanoparticles by atmospheric-pressure pulsed discharge plasma in a slug flow system. *Japanese Journal of Applied Physics* **2019,** *58* (1), 016001.
47. Joshi, R. P.; Thagard, S. M., Streamer-like electrical discharges in water: Part I. Fundamental mechanisms. *Plasma Chemistry and Plasma Processing* **2013,** *33* (1), 1-15.

Chapter 2. Synthesis of metal oxide nanoparticles under atmospheric-pressure pulsed discharge plasma in the slug flow system

2.1 Introduction

2.1.1 Metal oxide nanoparticles

Metal oxide nanoparticles have gained an increasing interest due to their significant change on properties when particle size is decreased to the nanoscale range[1]. Due to the high density and limited size of edges and corners on their surface, metal oxide nanoparticles have unique chemical and physical properties, which is also observed size-dependent[2]. With the size of metal oxide nanoparticles decreasing, an increasing number of surface and interface atoms generates strain or stress and adjoining structural perturbations[3]. The properties of magnetic, optical, electrical can be dependent on the specific size of the nanoparticles[4]. Especially, it is found that very small nanoparticles contain unusual structural disorder, modifying substantially the properties[5].

Because of their high surface area and properties of size-dependence, metal oxide nanoparticles have been applied in various applications in wide fields, such as catalysis, sensors, optics, medicine, and electronic materials[1, 6-7]. Allahverdiyev et al.[8] reviewed that TiO_2 and Ag_2O nanoparticles show great antimicrobial activity against drug-resistant bacteria and leishmania parasites. Teja et al.[9] also reviewed the applications of magnetic iron oxide nanoparticles in the fields of catalysis and biomedicine.

2.1.1.1 Cerium dioxide nanoparticles

Cerium is one of rare earth metals, showing potential for a wide range of applications[10]. It has two stable oxidation states, Ce^{4+} and Ce^{3+}, in which the electron orbitals are empty or partially occupied[11]. Due to the ability to release or uptake oxygen depending on the switch between Ce^{4+}/Ce^{3+} redox cycles, cerium oxide nanoparticles have an important property of high oxygen storage capacity[12]. Hence, they are widely applied in the medical and biological fields as antioxidants[13], possessing remarked catalytic activity[14-16]. The band gap energy of ceria is 3.2 eV, which makes it a photocatalyst sensitive to ultraviolet radiation[17]. Cerium dioxide (CeO_2) nanomaterials also exhibit a photovoltaic response, which is directly derived from the nanometric particles size. The material possesses excellent thermal stability, large pore volumes, and high surface areas[18-20], making it easily doped after synthesis while maintaining textural and mechanical integrity[21]. Many researches have reported that CeO_2 nanoparticle and doped CeO_2 nanomaterials show potential in photocatalysis and solar cell[22-27].

2.1.1.2 Magnesium oxide nanoparticles

Magnesium oxide (MgO) is an important inorganic material with a wide band-gap[28], being eco-friendly, economically feasible and industrially[29]. It has been studied for its inherent properties of high ionic character, simple stoichiometry, crystal structure, and surface structural defects[30]. MgO nanoparticles show excellent physicochemical

behaviors on stability, corrosion resistance[31], refractive index[32], thermal conductivity, dielectric resistance, and physical strength[33], etc. Therefore, MgO nanoparticles have been applied in various applications, including catalysis[34], semiconducting materials, electrochemical biosensors, refractory materials, absorbents[32, 35]. Thin films of magnesium oxide are also reported to be used for ultraviolet detection[36], heat spreader[37-38]. In addition, Mg^{2+} ions are ubiquitous and essential for living organisms, and they also show a biological activity for bone regeneration[39]. Hence MgO nanoparticles are also used in medicine, for the relief of heartburn, sore stomach, bone regeneration, tumor treatment, and antibacterial agent[30, 40-41]. Tang et al.[42] reported that MgO nanoparticles showed the excellent antibacterial activity against Lactobacillus plantarum.

2.1.1.3 Zinc oxide nanoparticles

Zinc oxide (ZnO) is known as a promising inorganic material, with a wide band gap of 3.3 eV, a high excitonic binding energy of 60 meV at room temperature[43], and a natural n-type electrical conductivity[44]. ZnO shows excellent behaviors on optical, chemical sensing, semiconductor, and electrical conductivity[45]. Due to the strong ionic boding in the Zn-O, ZnO has long durability, high selectivity, and heat resistance[46]. Hence it is used in various applications, such as laser diodes[47], transistors[48], phosphors[49], and piezoelectric transduces[50]. When particle size is reduced to the nanometer range, because of increased specific surface area and enhanced particle surface reactivity, ZnO nanoparticles exhibit high catalytic, high photochemical, and attractive antibacterial

properties[51]. Due to their biosafe and biocompatible properties[52], they are also used as antibacterial agents in food industry and medical fields[53]. Padmavathy et al.[46] reported that ZnO nanoparticles have great antibacterial activity, and the bactericidal efficacy increased with decreasing particle size.

2.1.2 Traditional methods of synthesizing metal oxide nanoparticles

Current methods to synthesize metal oxide nanoparticles mainly include hydrothermal[54-58], chemical precipitation[59-60], sol-gel technique[61-63], solvothermal[64], microwave[65], and thermal hydrolysis[66] methods. However, these methods usually require long reaction time and complicated steps. Gnanam et al.[67] reported the successful synthesis of CeO_2 nanoparticles by hydrothermal method, with a 10-hour reaction at 150°C. Ling et al.[61] reported the sol-gel method with the processes of stirring for 1h, heating in water bath, preferring for 4 h, and firing for 4 h. In addition, organic solvents and ligands are always required during the processed, increasing the environmental stress and the operating costs. The treatment capacity is also often limited by the tank reactor.

2.1.3 Synthesis of metal oxide nanoparticles using cold plasma

Cold plasma technology is an advanced oxidation process, generating reactive species with high reactivities in situ. Nanoparticles synthesis using cold plasma inherently does not require solvent and ligand, enabling the synthesis of nanocrystals

with high purity[68]. During the process of cold plasma, electrons also charge nanomaterials immersed in the plasma negatively, preventing the nanoparticles aggregation, which enables the synthesis of nanoparticles with narrow size distributions[68]. Electron collisions with molecules or atoms generate highly reactive growth precursors, leading to the largely irreversible nanoparticle growth process, enabling the nanoparticles be grown far from their chemical equilibrium and the efficient inclusions of dopants[68].

2.1.4 Motivation and purpose of this work

In this work, the slug flow system using pulsed discharge plasma is utilized to synthesize metal oxide nanoparticles under atmospheric-pressure conditions, providing an easy, continuous, and environmentally friendly process. Cerium nitrate, magnesium chloride, and zinc chloride aqueous solution are used as feed to synthesize cerium dioxide, magnesium oxide, zinc oxide nanoparticles, respectively. The products are characterized by different methods.

2.2 Experimental procedure

2.2.1 Materials

Cerium (III) nitrate ($Ce(NO_3)_3$) (Product No. 035-09735), magnesium chloride ($MgCl_2$) (Product No. 136-03995), zinc chloride ($ZnCl_2$) (Product No. 265-00275), starch (Product No. 191-03985) and distilled water (Product No. 049-16787) were

purchased from Wako Pure Chemical Industries, Ltd., Osaka, Japan. Argon (purity > 99.99%) was purchased from Sogo Kariya Sanso, Inc., Nagoya, Japan. All the chemicals used in this study were used as received without further purification. 1 mmol/L of $Ce(NO_3)_3$, $MgCl_2$, and $ZnCl_2$ were used as the feed solution, respectively. Starch of 0.1 wt% was added as the stabilizer in the feed solution when synthesizing cerium oxide nanoparticles.

2.2.2 Experimental methods

Figure 2.1 shows the schematic of the synthesis of metal oxide nanoparticles using atmospheric-pressure pulsed discharge plasma in a slug flow system. The slug flow system has been reported in the synthesis of silver nanoparticles[69] and gold nanoparticles[70]. Straight capillary tube (120 mm×2.0 mm i.d., Fujirika Kogyo Co., FPT-300, Osaka, Japan) was used as the slug flow reactor and residence time of plasma-state bubbles was approximately 3 s. Copper (Cu) sheets with a width of 10 mm were attached to the outer surface of the glass tube as electrodes. A high-voltage electrode and a ground electrode were arranged, and the distance between the adjacent electrodes was approximately 25 mm. The feed solution was introduced into the system using a high-performance liquid chromatography pump (LC-10AD, Shimadzu Co., Kyoto, Japan) and argon gas was introduced from a gas flowmeter (RK-1250, Kofloc Instruments Inc., Kyoto, Japan) into the system simultaneously through a T-type junction (SS-200-3, Swagelok). A high voltage was provided by an AC power supply (TE-HVP1510K300-NP, Tamaoki Electronics Co., Ltd., Kawaguchi, Japan). The

voltage and current of the system were observed using an oscilloscope (TDS2024C, Tektronix Inc., OR, USA).

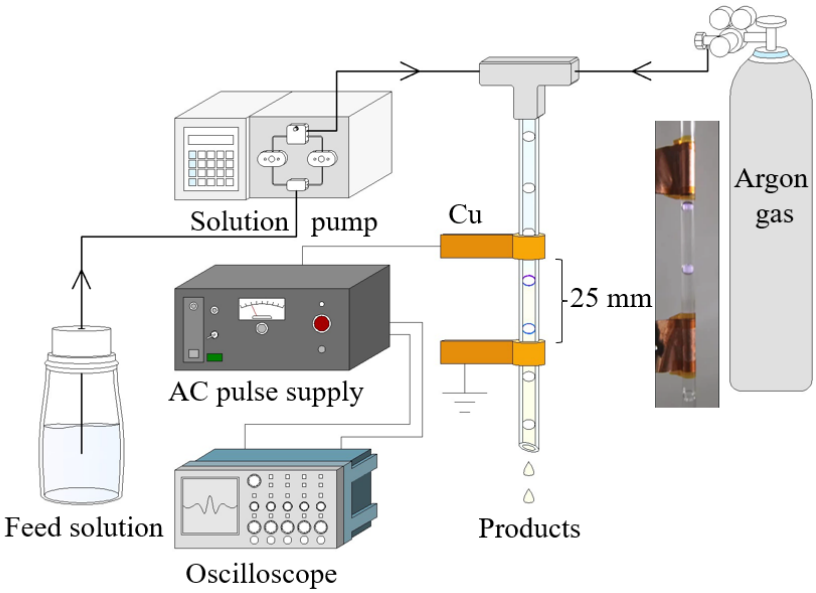

Figure 2.1 Apparatus scheme of synthesizing metal oxide nanoparticles by atmospheric-pressure pulsed discharge plasma

Bubbles were generated in the straight capillary glass tube, and adjusted by varying the flow rates of the gas and feed liquid solution. The flow rates of the feed solution and argon gas were approximately 1.5 and 0.15 mL/min, respectively. The system was powered by a high voltage of 10.0 kV (peak-to-peak). An AC pulse power supply was introduced into the system through the copper sheets attached to the outer glass tube to generate plasma. The discharge waveforms of voltage and current are shown in the Figure 2.2.

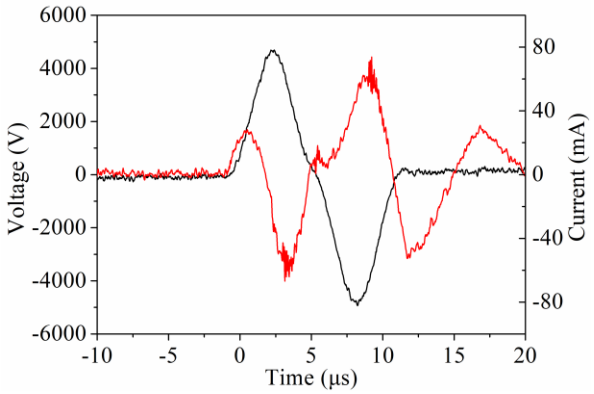

Figure 2.2 Voltage (black) and current (red) discharge waveforms

2.2.3 Analysis methods

Ultraviolet-visible spectrophotometer (UV-vis)

UV-vis is a method of qualitative and quantitative analysis, based on the absorption spectra obtained by irradiating the samples in a cell with the ultraviolet-visible region light. After absorbing UV-visible light, atoms and molecules undergo electronic excitation to higher-energy states. The chemical structures of atomic and molecular species can be identified from the wavelength of the light absorbed by them[60]. The results are expressed as absorbance or transmittance, and absorbance A can be calculated by the following equation based on Bouguer-Lambert-Beer law[71]:

$$A = -\log(\frac{I}{I_0})$$

where I_0 and I are the incident light intensity and transmitted light intensity, respectively.

In this study, the product solution containing different metal oxide nanoparticles is placed in a quartz cell and measured using an ultraviolet-visible spectrophotometer (V-550, Jasco Corporation, Japan). The samples are qualitatively analyzed according to

the characteristic peaks in the UV-vis spectra.

Transmission electron microscope (TEM)

TEM is usually observed the microstructure of the sample by irradiating a thin specimen with an electron beam of uniform current density. Electrons are emitted in the electron gun or filaments, then accelerated by electrostatic plates until reaches final voltage and enters the condenser lens system. The electron-intensity distribution behind the specimen is imaged onto a fluorescent screen with the lens system[72].

In this study, the product solution is dropped directly onto a copper-mesh grid NP-C15 (Ohken Shoji Co., Ltd., Tokyo, Japan) to prepare the samples. The samples are characterized by using a transmission electron microscope (JEM-2100Plus, Japan Electronic Co., Ltd.) at an acceleration voltage of 200 kV. The size distribution of nanoparticles is determined by using Nano Measurer software (Fudan Univ., Fudan, China), which is obtained by measuring more than 300 nanoparticles in several TEM images. The morphologies, growth patterns and crystal distributions of the samples are observed in the TEM images.

High resolution transmission electron microscope (HRTEM)

HRTEM has been effectively and widely used to analyze crystal structures and lattice imperfections in materials on an atomic scale[73]. The selected area electron diffraction (SAED) performed inside the HRTEM shows the diffraction pattern of the crystal structure of material in a specific chosen area[74]. In this study, the crystal structure

of the nanoparticles is examined through their HRTEM images and SAED patterns, obtained from a high-resolution transmission electron microscope (JEM-2100F, Japan Electronic Co., Ltd.). Lattice spacing and atomic image of the crystal can be observed.

Energy dispersive X-ray spectroscopy (EDS)

EDS is a method to analyze the elemental composition or chemical characterization of samples. Every element has the characteristic peaks on its electromagnetic emission spectrum due to its unique atomic structure. Sample is irradiated by a beam of electron to stimulate the emission of characteristic X-rays from a specimen, which could be measured by an energy-dispersive spectrometer. According to measured characteristic energies of the X-rays, the elemental composition of the specimen can be measured[75]. In this study, elemental composition of the metal oxide nanoparticles is analyzed using an energy dispersive X-ray spectroscopy (JEOL, JED-2300T & Gatan, GIF Quantum ER) installed in TEM (JEM-2100F, Japan Electronic Co., Ltd.).

2.3 Results and discussion

2.3.1 Characterization of cerium dioxide nanoparticles

As shown in Figure 2.3, a yellow solution containing cerium oxide nanoparticles was obtained after plasma treatment, and the Tyndall effect could be observed when the product was irradiated with a laser beam, which indicated that it contained well-

dispersed colloidal particles[76].

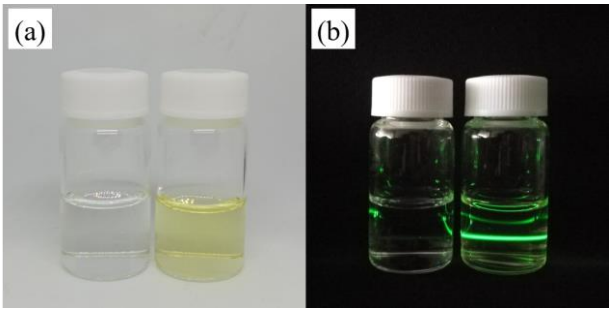

Figure 2.3 Photographs of feed solution (left) and product solution (right): (a) room lighting; (b)Tyndall effect in solutions

Figure 2.4 shows the EDS elemental maps of the cerium oxide nanoparticles synthesized in the slug flow system using pulsed discharge plasma. Ce and O were detected in the elemental maps, which indicates that the cerium oxide nanoparticles are generated through plasma-induced reactions in the slug flow system. Figure 2.5 shows the TEM images of the cerium oxide nanoparticles synthesized using 0.1 wt% starch as the stabilizer. The nanoparticles were uniform and tiny, with a mean size of approximately 3.4 nm.

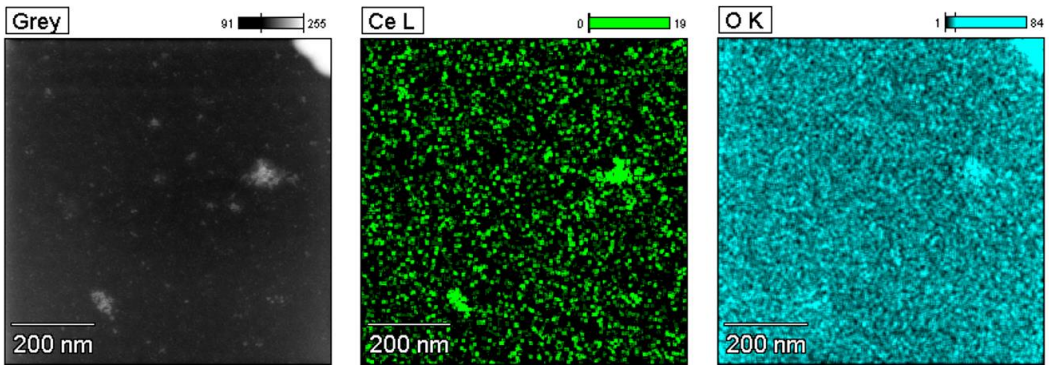

Figure 2.4 EDS mapping images of cerium oxide nanoparticles for cerium and oxygen

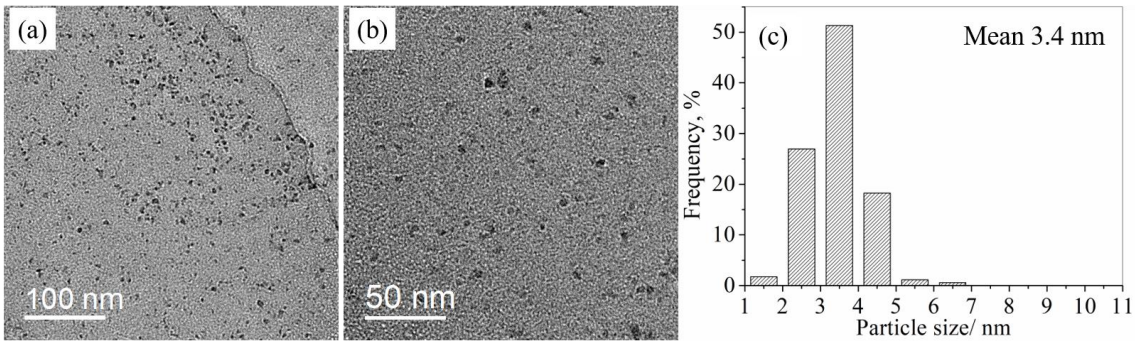

Figure 2.5 (a), (b) TEM images (c) particle size distributions of cerium oxide nanoparticles

The crystal structure of the cerium oxide nanoparticles was examined by obtaining their HRTEM images (Figure 2.6 a) and SAED patterns (Figure 2.6 b). The lattice spacing of the nanoparticles was 0.31 nm, as determined from their HRTEM images. According to Verma et al.[77], the spacing of 0.31 nm corresponds to the (111) planes of cubic CeO_2. Balaji et al.[27] also attributed the fringe spacing of 0.31 nm to the (111) plane of CeO_2 nanoparticles. As can be observed from Figure 2.6 b, the SAED pattern of the nanoparticles showed three diffraction rings corresponding to the (111), (220), and (311) planes of CeO_2 (JCPDS card no. 34-0394).

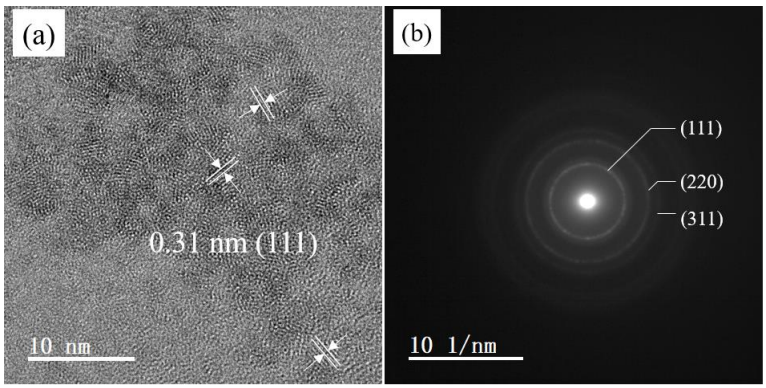

Figure 2.6 (a) HRTEM image and (b) SAED pattern of cerium oxide nanoparticles synthesized with starch as stabilizer

Figure 2.7 shows the UV-vis spectra of the feed solution and products after plasma treatment. In order to eliminate the interference of adding starch, 0.1 wt% starch solution was also analyzed. All the samples except starch showed absorbance peaks at approximately 250 and 300 nm. Wang et al.[78] reported that the absorbance peaks at around 250 and 300 nm were due to the charge transfer transition from the O^{2-}(2p) to Ce^{4+}(4f) orbitals in CeO_2. Babitha et al.[12] also reported similar peaks at 250 and 340 nm. The difference in the peak locations can be attributed to the difference in the particle sizes. Yin et al.[79] reported the blue shifts of the absorption peaks with a decrease in the size of CeO_2 nanoparticles. The products showed higher absorbance intensity, indicating the presence of CeO_2 nanoparticles in them. The absorbance peak intensity of the CeO_2 nanoparticles increased with the addition of the stabilizer added, indicating the stabilizer addition may be beneficial for generating CeO_2 nanoparticles in this system investigated in this study.

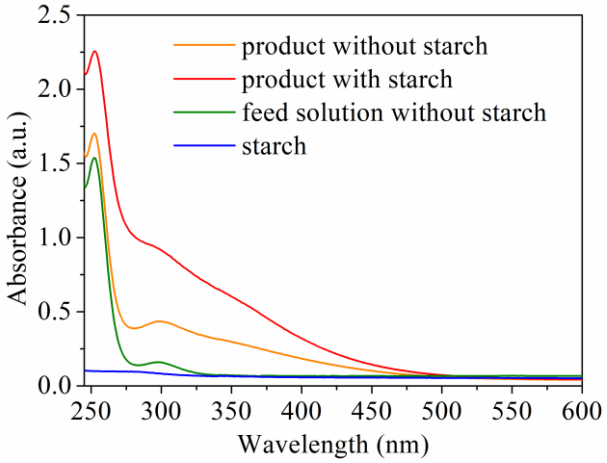

Figure 2.7 UV-vis spectra of feed solution and solution products containing CeO_2 nanoparticles

2.3.2 Characterization of magnesium oxide nanoparticles

$MgCl_2$ of 1 mmol/L without a stabilizer was used as the feed solution, and product after plasma treatment was subjected to characterization analyses. As Figure 2.8 shown, tiny nanoparticles were also observed in the TEM images at different magnifications. According to the results of EDS spectrum in Figure 2.9, the peaks corresponding to Mg could be clearly observed. Mg and O were also detected in the elemental maps, indicating that magnesium oxide nanoparticles were generated in the slug flow system through gas/liquid plasma.

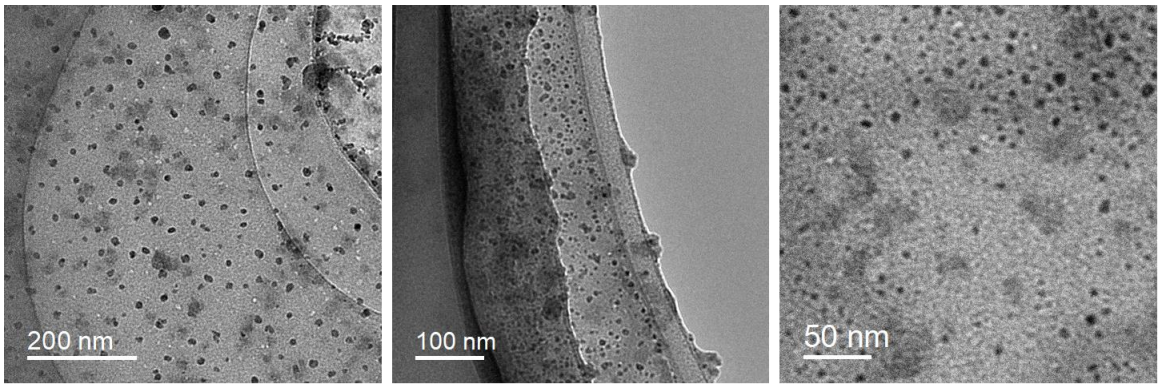

Figure 2.8 TEM images of MgO nanoparticles

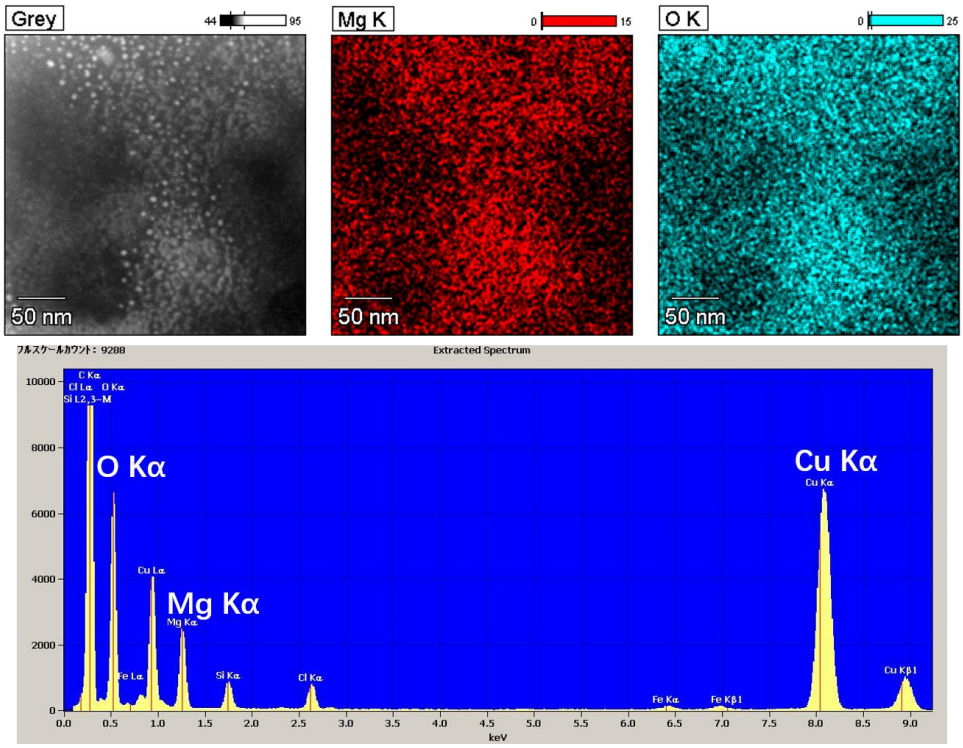

Figure 2.9 Grey TEM image of MgO nanoparticles with the corresponding EDS mapping images and spectrum

The crystal structure of MgO nanoparticles was examined by obtaining their HRTEM image and SAED pattern, shown in Figure 2.10. As measured from the HRTEM image, the lattice spacing of the MgO nanoparticles was 0.25 nm, which is corresponding to the (111) plane of MgO[80]. Peng et al.[81] also reported that the lattice spacing of 0.245 nm matched well with MgO (111) planes. As shown in the SAED pattern, the diffraction rings from inner to outer corresponds to the (111) and (200) diffraction of MgO.

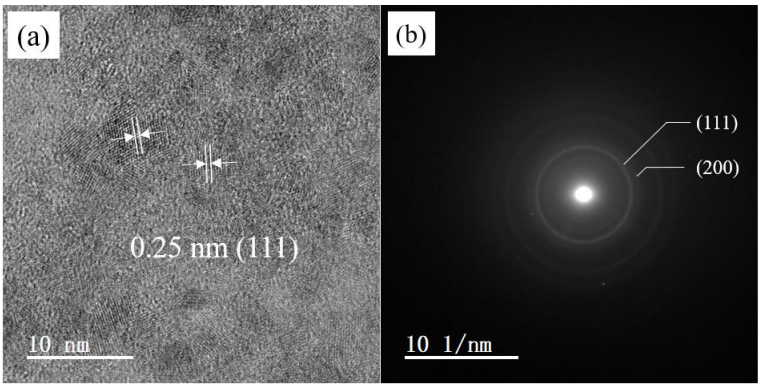

Figure 2.10 (a) HRTEM image and (b) SAED pattern of MgO nanoparticles

2.3.3 Characterization of zinc oxide nanoparticles

$ZnCl_2$ of 1 mmol/L without a stabilizer was used as the feed solution, and product after plasma treatment was subjected to characterization analyses. The morphology of product was examined by TEM, shown in Figure 2.11. Cubic nanoparticles were observed in the TEM images, but the nanoparticles were ununiform without a stabilizer. In addition, amorphous flakes generated. The elemental composition of the product was analyzed by EDS. As shown in Figure 2.12, the peaks corresponding to Zn could be clearly observed. Zn and O were also detected in the elemental maps, indicating that zinc oxide nanoparticles are produced using discharge plasma in this slug flow system.

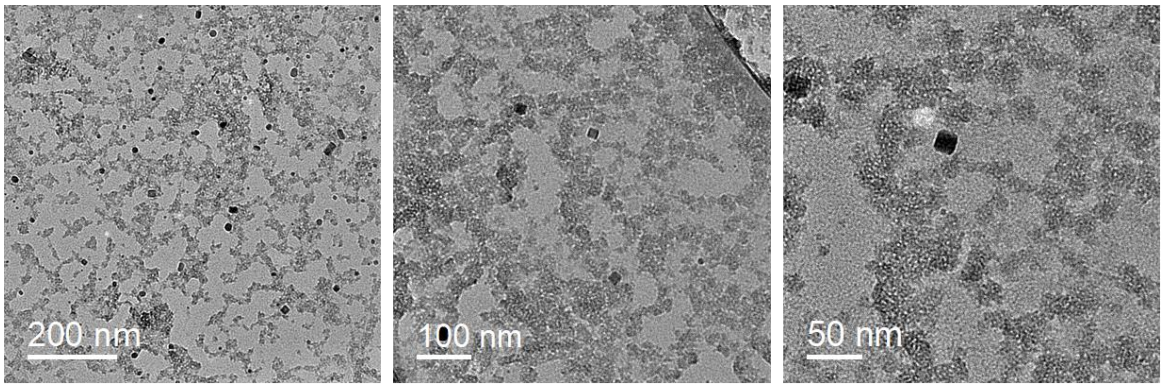

Figure 2.11 TEM images of ZnO nanoparticles

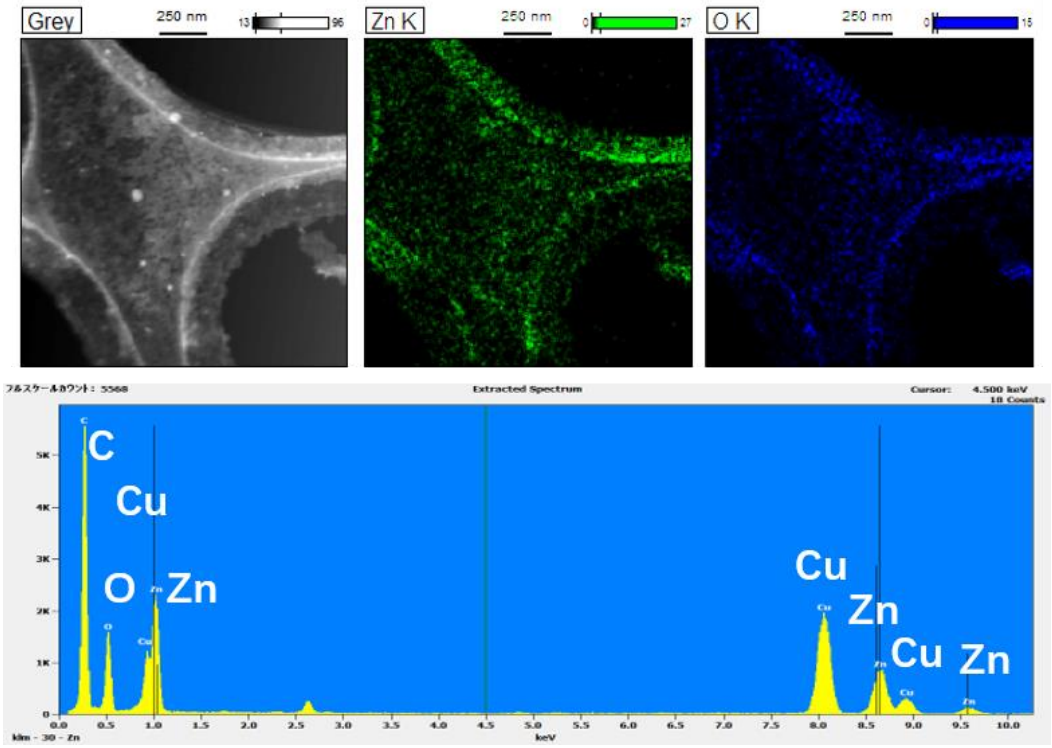

Figure 2.12 Grey TEM image of ZnO nanoparticles with the EDS mapping images and spectrum

Primc et al.[82] reviewed that chemically reactive species with a potential energy could be formed under thermodynamical nonequilibrium conditions, interacting readily with the Zn precursors and initiating the reactions to generate nanoparticles or

nanowires. Zhang et al.[83] reported the successful synthesis of ZnO nanosheet-assembly film with larger specific surface area using cold plasma, which is generated by air dielectric barrier discharge. Ananth et al.[84] reported a soft jet plasma-assisted method of preparing ZnO nanomaterials, exhibiting variety of surface morphology. Shutov et al.[85] proposed the plasma-solution system to synthesize ZnO powders with a hexagonal shape crystal.

2.4 Conclusion

In this study, cerium nitrate, magnesium chloride, and zinc chloride aqueous solutions were used as the feed solution to synthesize corresponding metal oxide nanoparticles in the slug flow system using pulsed discharge plasma under atmospheric-pressure conditions, respectively. Compared with traditional methods, the slug flow system provided a uniform and continuous reaction field, beneficial for nanoparticles synthesis. Results showed that cerium dioxide nanoparticles, magnesium oxide nanoparticles, and zinc oxide nanoparticles were synthesized successfully in the slug flow system using gas/liquid pulsed discharge plasma. Among them, cerium dioxide nanoparticles were selected as the target product to investigate the reaction mechanism and effect of different experimental factors in next Chapter.

References

1. Mallakpour, S.; Madani, M., A review of current coupling agents for modification of metal oxide nanoparticles. *Progress in Organic Coatings* **2015,** *86*, 194-207.
2. Liu, W.-T., Nanoparticles and their biological and environmental applications. *Journal of bioscience and bioengineering* **2006,** *102* (1), 1-7.
3. Chavali, M. S.; Nikolova, M. P., Metal oxide nanoparticles and their applications in nanotechnology. *SN Applied Sciences* **2019,** *1* (6), 607.
4. Oskam, G., Metal oxide nanoparticles: synthesis, characterization and application. *Journal of sol-gel science and technology* **2006,** *37* (3), 161-164.
5. Gilbert, B.; Huang, F.; Zhang, H.; Waychunas, G. A.; Banfield, J. F., Nanoparticles: strained and stiff. *Science* **2004,** *305* (5684), 651-654.
6. Fernández-Garcia, M.; RODGRIGUEZ, J. *Metal oxide nanoparticles*; Brookhaven National Lab.(BNL), Upton, NY (United States): 2007.
7. Stoimenov, P. K.; Klinger, R. L.; Marchin, G. L.; Klabunde, K. J., Metal oxide nanoparticles as bactericidal agents. *Langmuir* **2002,** *18* (17), 6679-6686.
8. Allahverdiyev, A. M.; Abamor, E. S.; Bagirova, M.; Rafailovich, M., Antimicrobial effects of TiO2 and Ag2O nanoparticles against drug-resistant bacteria and leishmania parasites. *Future microbiology* **2011,** *6* (8), 933-940.
9. Teja, A. S.; Koh, P.-Y., Synthesis, properties, and applications of magnetic iron oxide nanoparticles. *Progress in Crystal Growth and Characterization of Materials* **2009,** *55* (1), 22-45.
10. Kyosseva, S. V.; Mc Ginnis, J. F., Cerium oxide nanoparticles as promising ophthalmic therapeutics for the treatment of retinal diseases. *World* **2015,** *1*.
11. Ma, W.; Mashimo, T.; Tamura, S.; Tokuda, M.; Yoda, S.; Tsushida, M.; Koinuma, M.; Kubota, A.; Isobe, H.; Yoshiasa, A., Cerium oxide (CeO2-x) nanoparticles with high Ce3+ proportion synthesized by pulsed plasma in liquid. *Ceramics International* **2020,** *46* (17), 26502-26510.
12. Stetsovych, V.; Pagliuca, F.; Dvořák, F.; Duchoň, T.; Vorokhta, M.; Aulická, M.; Lachnitt, J.; Schernich, S.; Matolínová, I.; Veltruská, K.; Skála, T.; Mazur, D.; Mysliveček, J.; Libuda, J.; Matolín, V., Epitaxial Cubic Ce2O3 Films via Ce–CeO2 Interfacial Reaction. *The Journal of Physical Chemistry Letters* **2013,** *4* (6), 866-871.
13. Estevez, A. Y.; Ganesana, M.; Trentini, J. F.; Olson, J. E.; Li, G.; Boateng, Y. O.; Lipps, J. M.; Yablonski, S. E.; Donnelly, W. T.; Leiter, J. C., Antioxidant Enzyme-Mimetic Activity and Neuroprotective Effects of cerium oxide nanoparticles stabilized with various ratios of citric acid and EDTA. *Biomolecules* **2019,** *9* (10), 562.
14. Das, S.; Dowding, J. M.; Klump, K. E.; McGinnis, J. F.; Self, W.; Seal, S., Cerium oxide nanoparticles: applications and prospects in nanomedicine. *Nanomedicine* **2013,** *8* (9), 1483-1508.
15. Hirst, S. M.; Karakoti, A. S.; Tyler, R. D.; Sriranganathan, N.; Seal, S.; Reilly, C. M., Anti-inflammatory Properties of Cerium Oxide Nanoparticles. *Small* **2009,** *5* (24), 2848-2856.
16. Hao, X.; Yoko, A.; Chen, C.; Inoue, K.; Saito, M.; Seong, G.; Takami, S.; Adschiri,

T.; Ikuhara, Y., Atomic‐Scale Valence State Distribution inside Ultrafine CeO2 Nanocubes and Its Size Dependence. *Small* **2018,** *14* (42), 1802915.
17. Li, B.; Gu, T.; Ming, T.; Wang, J.; Wang, P.; Wang, J.; Yu, J. C., (Gold Core)@(Ceria Shell) Nanostructures for Plasmon-Enhanced Catalytic Reactions under Visible Light. *ACS Nano* **2014,** *8* (8), 8152-8162.
18. Calvache-Muñoz, J.; Prado, F. A.; Rodríguez-Páez, J. E., Cerium oxide nanoparticles: Synthesis, characterization and tentative mechanism of particle formation. *Colloids and Surfaces A: Physicochemical and Engineering Aspects* **2017,** *529*, 146-159.
19. Caputo, F.; De Nicola, M.; Sienkiewicz, A.; Giovanetti, A.; Bejarano, I.; Licoccia, S.; Traversa, E.; Ghibelli, L., Cerium oxide nanoparticles, combining antioxidant and UV shielding properties, prevent UV-induced cell damage and mutagenesis. *Nanoscale* **2015,** *7* (38), 15643-15656.
20. Dhall, A.; Self, W., Cerium oxide nanoparticles: a brief review of their synthesis methods and biomedical applications. *Antioxidants* **2018,** *7* (8), 97.
21. Corma, A.; Atienzar, P.; Garcia, H.; Chane-Ching, J.-Y., Hierarchically mesostructured doped CeO2 with potential for solar-cell use. *Nature materials* **2004,** *3* (6), 394-397.
22. Liyanage, A. D.; Perera, S. D.; Tan, K.; Chabal, Y.; Balkus, K. J., Synthesis, Characterization, and Photocatalytic Activity of Y-Doped CeO2 Nanorods. *ACS Catalysis* **2014,** *4* (2), 577-584.
23. Mittal, M.; Gupta, A.; Pandey, O., Role of oxygen vacancies in Ag/Au doped CeO2 nanoparticles for fast photocatalysis. *Solar Energy* **2018,** *165*, 206-216.
24. Xu, B.; Yang, H.; Zhang, Q.; Yuan, S.; Xie, A.; Zhang, M.; Ohno, T., Design and Synthesis of Sm, Y, La and Nd‐doped CeO2 with a broom‐like hierarchical structure: a photocatalyst with enhanced oxidation performance. *ChemCatChem* **2020,** *12* (9), 2638-2646.
25. Channei, D.; Inceesungvorn, B.; Wetchakun, N.; Ukritnukun, S.; Nattestad, A.; Chen, J.; Phanichphant, S., Photocatalytic degradation of methyl orange by CeO2 and Fe–doped CeO2 films under visible light irradiation. *Scientific Reports* **2014,** *4* (1), 1-7.
26. Meng, R.; Feng, X.; Yang, Y.; Lv, X.; Cao, J.; Tang, Y., Cerium-oxide-modified anodes for efficient and UV-stable ZnO-based perovskite solar cells. *ACS applied materials & interfaces* **2019,** *11* (14), 13273-13278.
27. Balaji, S.; Mandal, B. K.; Vinod Kumar Reddy, L.; Sen, D., Biogenic Ceria Nanoparticles (CeO2 NPs) for Effective Photocatalytic and Cytotoxic Activity. *Bioengineering* **2020,** *7* (1).
28. Al-Gaashani, R.; Radiman, S.; Al-Douri, Y.; Tabet, N.; Daud, A. R., Investigation of the optical properties of Mg(OH)2 and MgO nanostructures obtained by microwave-assisted methods. *Journal of Alloys and Compounds* **2012,** *521*, 71-76.
29. Abinaya, S.; Kavitha, H. P.; Prakash, M.; Muthukrishnaraj, A., Green synthesis of magnesium oxide nanoparticles and its applications: A review. *Sustainable Chemistry*

and Pharmacy **2021,** *19*, 100368.
30. Bindhu, M.; Umadevi, M.; Micheal, M. K.; Arasu, M. V.; Al-Dhabi, N. A., Structural, morphological and optical properties of MgO nanoparticles for antibacterial applications. *Materials Letters* **2016,** *166*, 19-22.
31. Shen, Y.; He, L.; Yang, Z.; Xiong, Y., Corrosion behavior of different coatings prepared on the surface of AZ80 magnesium alloy in simulated body fluid. *Journal of Materials Engineering and Performance* **2020,** *29* (3), 1609-1621.
32. Hornak, J.; Trnka, P.; Kadlec, P.; Michal, O.; Mentlík, V.; Šutta, P.; Csányi, G. M.; Tamus, Z. Á., Magnesium oxide nanoparticles: dielectric properties, surface functionalization and improvement of epoxy-based composites insulating properties. *Nanomaterials* **2018,** *8* (6), 381.
33. Khalil, K. D.; Bashal, A. H.; Khalafalla, M.; Zaki, A. A., Synthesis, structural, dielectric and optical properties of chitosan-MgO nanocomposite. *Journal of Taibah University for Science* **2020,** *14* (1), 975-983.
34. Lee, E.-K.; Jung, K.-D.; Joo, O.-S.; Shul, Y.-G., Magnesium oxide as an effective catalyst in catalytic wet oxidation of H2S to sulfur. *Reaction Kinetics and Catalysis Letters* **2004,** *82* (2), 241-246.
35. Tang, Z.-X.; Lv, B.-F., MgO nanoparticles as antibacterial agent: preparation and activity. *Brazilian Journal of Chemical Engineering* **2014,** *31* (3), 591-601.
36. Yang, C.-C.; Chen, K.-Y.; Yeh, W.-S.; Su, Y.-K.; Wang, Z.-H., Ultraviolet Photodetection Application in Magnesium Indium Oxide Thin Film Transistors via Co-Sputtering Deposition. *Applied Sciences* **2020,** *10* (15), 5128.
37. Idris, M. S.; Subramani, S., Performance of 9.0 W light-emitting diode on various layers of magnesium oxide thin film thermal interface material. *Applied Physics A* **2020,** *126* (8), 1-13.
38. Idris, M. S.; Shanmugan, S.; Devarajan, M.; Maryam, W., Heat transfer enhancement in light - emitting diode packaging employing different molar concentration of magnesium oxide thin films as a heat spreader. *International Journal of Energy Research* **2020,** *44* (12), 9527-9537.
39. Martinez-Boubeta, C.; Balcells, L.; Cristòfol, R.; Sanfeliu, C.; Rodríguez, E.; Weissleder, R.; Lope-Piedrafita, S.; Simeonidis, K.; Angelakeris, M.; Sandiumenge, F.; Calleja, A.; Casas, L.; Monty, C.; Martínez, B., Self-assembled multifunctional Fe/MgO nanospheres for magnetic resonance imaging and hyperthermia. *Nanomedicine: Nanotechnology, Biology and Medicine* **2010,** *6* (2), 362-370.
40. Krishnamoorthy, K.; Moon, J. Y.; Hyun, H. B.; Cho, S. K.; Kim, S.-J., Mechanistic investigation on the toxicity of MgO nanoparticles toward cancer cells. *Journal of materials chemistry* **2012,** *22* (47), 24610-24617.
41. Pugazhendhi, A.; Prabhu, R.; Muruganantham, K.; Shanmuganathan, R.; Natarajan, S., Anticancer, antimicrobial and photocatalytic activities of green synthesized magnesium oxide nanoparticles (MgONPs) using aqueous extract of Sargassum wightii. *Journal of Photochemistry and Photobiology B: Biology* **2019,** *190*, 86-97.
42. Tang, Z.-X.; Fang, X.-J.; Zhang, Z.-L.; Zhou, T.; Zhang, X.-Y.; Shi, L.-E., Nanosize MgO as antibacterial agent: preparation and characteristics. *Brazilian Journal of*

Chemical Engineering **2012,** *29* (4), 775-781.
43. Zhang, Y.; Ram, M. K.; Stefanakos, E. K.; Goswami, D. Y., Synthesis, characterization, and applications of ZnO nanowires. *Journal of Nanomaterials* **2012,** *2012*.
44. Wellings, J. S.; Chaure, N. B.; Heavens, S. N.; Dharmadasa, I. M., Growth and characterisation of electrodeposited ZnO thin films. *Thin Solid Films* **2008,** *516* (12), 3893-3898.
45. Fan, Z.; Lu, J. G., Zinc oxide nanostructures: synthesis and properties. *Journal of nanoscience and nanotechnology* **2005,** *5* (10), 1561-1573.
46. Padmavathy, N.; Vijayaraghavan, R., Enhanced bioactivity of ZnO nanoparticles—an antimicrobial study. *Science and technology of advanced materials* **2008**.
47. Lee, S. Y.; Shim, E. S.; Kang, H. S.; Pang, S. S.; Kang, J. S., Fabrication of ZnO thin film diode using laser annealing. *Thin Solid Films* **2005,** *473* (1), 31-34.
48. Fortunato, E.; Barquinha, P.; Pimentel, A.; Gonçalves, A.; Marques, A.; Pereira, L.; Martins, R., Recent advances in ZnO transparent thin film transistors. *Thin Solid Films* **2005,** *487* (1), 205-211.
49. Hosono, E.; Fujihara, S.; Kimura, T., Low-temperature deposition of nanocrystalline ZnO phosphor films from neutral ethanolic zinc acetate solutions in the absence of base. *Electrochemical and solid-state letters* **2004,** *7* (4), C49.
50. Look, D. C., Recent advances in ZnO materials and devices. *Materials Science and Engineering: B* **2001,** *80* (1), 383-387.
51. Sirelkhatim, A.; Mahmud, S.; Seeni, A.; Kaus, N. H. M.; Ann, L. C.; Bakhori, S. K. M.; Hasan, H.; Mohamad, D., Review on zinc oxide nanoparticles: antibacterial activity and toxicity mechanism. *Nano-micro letters* **2015,** *7* (3), 219-242.
52. Wang, Z. L.; Song, J., Piezoelectric nanogenerators based on zinc oxide nanowire arrays. *Science* **2006,** *312* (5771), 242-246.
53. Raghupathi, K. R.; Koodali, R. T.; Manna, A. C., Size-dependent bacterial growth inhibition and mechanism of antibacterial activity of zinc oxide nanoparticles. *Langmuir* **2011,** *27* (7), 4020-4028.
54. Zhou, Y. C.; Rahaman, M. N., Hydrothermal synthesis and sintering of ultrafine CeO~ 2 powders. *Journal of materials research* **1993,** *8* (5), 1680-1686.
55. Hirano, M.; Kato, E., Hydrothermal Synthesis of Cerium(IV) Oxide. *Journal of the American Ceramic Society* **1996,** *79* (3), 777-780.
56. Ding, Y.; Zhang, G.; Wu, H.; Hai, B.; Wang, L.; Qian, Y., Nanoscale magnesium hydroxide and magnesium oxide powders: control over size, shape, and structure via hydrothermal synthesis. *Chemistry of materials* **2001,** *13* (2), 435-440.
57. Mutinda, S. Hydrothermal synthesis of shape/size-controlled cerium-based oxides. 2013.
58. Kepenekci, Ö. Hydrothermal Preparation of Single Crystalline CeO 2 Nanoparticles and The Influence of Alkali Hydroxides on Their Structure and Optical Behavior. Izmir Institute of Technology (Turkey), 2009.
59. Ketzial, J. J.; Nesaraj, A. S., Synthesis of CeO 2 nanoparticles by chemical precipitation and the effect of a surfactant on the distribution of particle sizes. *Journal of Ceramic Processing Research* **2011,** *12* (1), 74-79.

60. Babitha, K.; Sreedevi, A.; Priyanka, K.; Sabu, B.; Varghese, T., Structural characterization and optical studies of CeO2 nanoparticles synthesized by chemical precipitation. *Indian Journal of Pure & Applied Physics (IJPAP)* **2015,** *53* (9), 596-603.
61. Li, L.; Yang, H. K.; Moon, B. K.; Fu, Z.; Guo, C.; Jeong, J. H.; Yi, S. S.; Jang, K.; Lee, H. S., Photoluminescence Properties of CeO2:Eu3+ Nanoparticles Synthesized by a Sol-Gel Method. *The Journal of Physical Chemistry C* **2009,** *113* (2), 610-617.
62. Wang, J.; Novaro, O.; Bokhimi, X.; Lopez, T.; Gomez, R.; Navarrete, J.; Llanos, M.; Lopez-Salinas, E., Structural defects and acidic and basic sites in Sol− Gel MgO. *The Journal of Physical Chemistry B* **1997,** *101* (38), 7448-7451.
63. Yahya, N.; Daud, H.; Tajuddin, N. A.; Daud, H. M.; Shafie, A.; Puspitasari, P. In *Application of ZnO nanoparticles EM wave detector prepared by sol-gel and self-combustion techniques*, Journal of Nano Research, Trans Tech Publ: 2010; pp 25-34.
64. Su, Y.; Yang, W.; Sun, W.; Li, Q.; Shang, J. K., Synthesis of mesoporous cerium–zirconium binary oxide nanoadsorbents by a solvothermal process and their effective adsorption of phosphate from water. *Chemical Engineering Journal* **2015,** *268*, 270-279.
65. Shirke, B.; Patil, A.; Hankare, P.; Garadkar, K., Synthesis of cerium oxide nanoparticles by microwave technique using propylene glycol as a stabilizing agent. *Journal of Materials Science: Materials in Electronics* **2011,** *22* (2), 200-203.
66. Hirano, M.; Fukuda, Y.; Iwata, H.; Hotta, Y.; Inagaki, M., Preparation and spherical agglomeration of crystalline cerium (IV) oxide nanoparticles by thermal hydrolysis. *Journal of the American Ceramic Society* **2000,** *83* (5), 1287-1289.
67. Gnanam, S.; Gajendiran, J.; Ramana Ramya, J.; Ramachandran, K.; Gokul Raj, S., Glycine-assisted hydrothermal synthesis of pure and europium doped CeO2 nanoparticles and their structural, optical, photoluminescence, photocatalytic and antibacterial properties. *Chemical Physics Letters* **2021,** *763*, 138217.
68. Kortshagen, U. R.; Sankaran, R. M.; Pereira, R. N.; Girshick, S. L.; Wu, J. J.; Aydil, E. S., Nonthermal Plasma Synthesis of Nanocrystals: Fundamental Principles, Materials, and Applications. *Chemical Reviews* **2016,** *116* (18), 11061-11127.
69. Yamada, M.; Takahashi, S.; Wahyudiono; Takada, N.; Kanda, H.; Goto, M., Synthesis of silver nanoparticles by atmospheric-pressure pulsed discharge plasma in a slug flow system. *Japanese Journal of Applied Physics* **2019,** *58* (1), 016001.
70. Yamada, M.; Wahyudiono; Machmudah, S.; Kanda, H.; Zhao, Y.; Goto, M., Atmospheric-Pressure Pulsed Discharge Plasma in a Slug Flow Reactor System for the Synthesis of Gold Nanoparticles. *ACS omega* **2020,** *5* (28), 17679-17685.
71. Förster, H., UV/vis spectroscopy. *Characterization I* **2004**, 337-426.
72. Reimer, L., Transmission electron microscopy: physics of image formation and microanalysis. Springer: 2013; Vol. 36.
73. Horiuchi, S.; He, L., High-resolution transmission electron microscopy. *Kyoritsu* **1988,** *2*, 14.
74. Ayoola, H. O.; House, S. D.; Bonifacio, C. S.; Kisslinger, K.; Saidi, W. A.; Yang, J. C., Evaluating the accuracy of common γ-Al2O3 structure models by selected area electron diffraction from high-quality crystalline γ-Al2O3. *Acta Materialia* **2020,** *182*,

257-266.
75. Hodoroaba, V.-D., Energy-dispersive X-ray spectroscopy (EDS). In *Characterization of Nanoparticles*, Elsevier: 2020; pp 397-417.
76. Masui, T.; Hirai, H.; Imanaka, N.; Adachi, G.; Sakata, T.; Mori, H., Synthesis of cerium oxide nanoparticles by hydrothermal crystallization with citric acid. *Journal of Materials Science Letters* **2002,** *21* (6), 489-491.
77. Verma, R.; Samdarshi, S. K.; Bojja, S.; Paul, S.; Choudhury, B., A novel thermophotocatalyst of mixed-phase cerium oxide (CeO2/Ce2O3) homocomposite nanostructure: Role of interface and oxygen vacancies. *Solar Energy Materials and Solar Cells* **2015,** *141*, 414-422.
78. Wang, Z.; Quan, Z.; Lin, J., Remarkable Changes in the Optical Properties of CeO2 Nanocrystals Induced by Lanthanide Ions Doping. *Inorganic Chemistry* **2007,** *46* (13), 5237-5242.
79. Yin, L.; Wang, Y.; Pang, G.; Koltypin, Y.; Gedanken, A., Sonochemical Synthesis of Cerium Oxide Nanoparticles—Effect of Additives and Quantum Size Effect. *Journal of Colloid and Interface Science* **2002,** *246* (1), 78-84.
80. Zhu, K.; Hu, J.; Kuebel, C.; Richards, R., Efficient preparation and catalytic activity of MgO (111) nanosheets. *Angewandte Chemie International Edition* **2006,** *45* (43), 7277-7281.
81. Peng, Q.; Dai, Y.; Liu, K.; Luo, X.; He, D.; Tang, X.; Huang, G., A novel carbon nanotube–magnesium oxide composite with excellent recyclability to efficiently activate peroxymonosulfate for Rhodamine B degradation. *Journal of Materials Science* **2020,** *55* (25), 11267-11283.
82. Primc, G.; Brenčič, K.; Mozetič, M.; Gorjanc, M., Recent Advances in the Plasma-Assisted Synthesis of Zinc Oxide Nanoparticles. *Nanomaterials* **2021,** *11* (5), 1191.
83. Zhang, W.; Li, C.; Tian, Z.; Wang, Y.; Hou, Z., Preparation of ZnO nanosheet-assembly film on zinc plate by cold plasma. *Thin Solid Films* **2020,** *712*, 138274.
84. Ananth, A.; Dharaneedharan, S.; Seo, H.-J.; Heo, M.-S.; Boo, J.-H., Soft jet plasma-assisted synthesis of Zinc oxide nanomaterials: Morphology controls and antibacterial activity of ZnO. *Chemical Engineering Journal* **2017,** *322*, 742-751.
85. Shutov, D.; Rybkin, V.; Ivanov, A.; Smirnova, K., Synthesis of zinc oxide powders in plasma–solution systems. *High Energy Chemistry* **2017,** *51* (1), 65-69.

Chapter 3. Synthesis mechanism of cerium dioxide nanoparticles and effect of experimental conditions

3.1 Introduction

3.1.1 Cerium oxide nanoparticles

As mentioned in Chapter 2, cerium oxide nanoparticles have been applied in various applications of wide field because of their inherent properties. Due to the ability to switch between Ce^{4+}/Ce^{3+} redox cycles, cerium oxide nanoparticles were selected as the target product to investigate the reaction mechanism and effect of different experimental factors. Many researches have reported various methods to synthesize CeO_2 nanoparticles, including hydrothermal[1-2], chemical precipitation[3], solvothermal[4], and thermal hydrolysis[5]. But the researches of synthesizing Ce_2O_3 nanoparticles are rather limited. Ce_2O_3 is also a remarkable material, which has been applied virous applications, including catalysis[6-8], sensors[9], and thermal agent. Nadaroglu et al. reported[10] that Ce_2O_3 nanoparticles had antioxidants and anti-bacterial ability, showing the potential for commercial applications. It was also reported that the composite nanomaterials with Ce_2O_3 showed excellent antimicrobial[11] and catalytic activity[12], applied in the fields of food, medicine, and engineering. It is easier for Ce^{4+} ions to undergo strong hydration because of their low basicity and high charge[13]. Ce^{3+} ions tend to convert into Ce^{4+} ions in the presence of oxidative species during hydrolysis process. Therefore, it is difficult to synthesize Ce_2O_3 through the traditional methods. The method using cold plasma allows the synthesis of Ce_2O_3 nanoparticle, because of

the generation of hydrogen radicals with strongly reductive activity during the process.

3.1.2 Synthesis of cerium oxide nanoparticles using cold plasma

The methods using cold plasma provide a potential direction to synthesize metal oxide nanoparticles, environmentally friendly and easy implemented. Lin et al[14] reported the successful synthesis of europium doped ceria nanoparticles in a gas/liquid plasma system powered by a DC supply, obtaining high purity crystalline. Ma et al.[15] reported the method using pulsed plasma in liquid to synthesize cerium oxide nanoparticles, showing high photocatalytic activity, which may attribute to the high Ce^{3+} proportion (42.2%) and the small particles size of 3 nm.

3.1.3 Motivation and purpose of this work

In this study, the slug flow system using pulsed discharge plasma is utilized to synthesize cerium oxide nanoparticles under atmospheric-pressure conditions. In order to increase the concentration of generating nanoparticles, a circular capillary glass tube coil is used as the slug flow reactor. Compared with the straight capillary glass tube used in Chapter 2, residence time is prolonged and electrodes number is increased, and effect of different slug flow reactor on synthesized nanoparticles is studied. The reaction mechanism of synthesizing cerium dioxide nanoparticles is studied, and the effect of other experimental factors is also investigated. Ammonium cerium (IV) nitrate is used as cerium source to attempt to synthesize Ce_2O_3 nanoparticles.

3.2 Experimental procedure

3.2.1 Materials

Cerium (III) nitrate ($Ce(NO_3)_3$) (Product No. 035-09735), ammonium cerium (IV) nitrate ($(NH_4)_2Ce(NO_3)_6$) (Product No. 038-01741), starch (Product No. 191-03985) and distilled water (Product No. 049-16787) were purchased from Wako Pure Chemical Industries, Ltd., Osaka, Japan. Argon (purity > 99.99%) was purchased from Sogo Kariya Sanso, Inc., Nagoya, Japan. All the chemicals used in this study were used as received without further purification. The feed solution was prepared with a mixture of $Ce(NO_3)_3$ (1 mmol/L) and starch (0.10 – 0.40 wt%) aqueous solution.

3.2.2 Experimental methods

Figure 3.1 shows the schematic of the synthesis of CeO_2 by atmospheric-pressure pulsed discharge plasma in the slug flow system. Similar to the system in Chapter 2, in this study, a circular capillary glass tube coil (2.0 m × 1.8 mm i.d., G-3000, Shimadzu Co., Kyoto, Japan) was used as the slug flow reactor. Five high-voltage electrodes and ten ground electrodes were arranged, and the distance between the adjacent electrodes was approximately 25 mm. Residence time of plasma-state bubbles was prolonged approximately 3 minutes. The effect of the different reactors will be discussed later. Starch with a concentration of 0.1-0.4 wt% was added as a stabilizer into the feed solution. The flow rates of the feed solution and argon gas were also set at

approximately 1.5 and 0.15 mL/min, respectively. A high voltage of 10.0 kV (peak-to-peak) was introduced into the system to generate plasma.

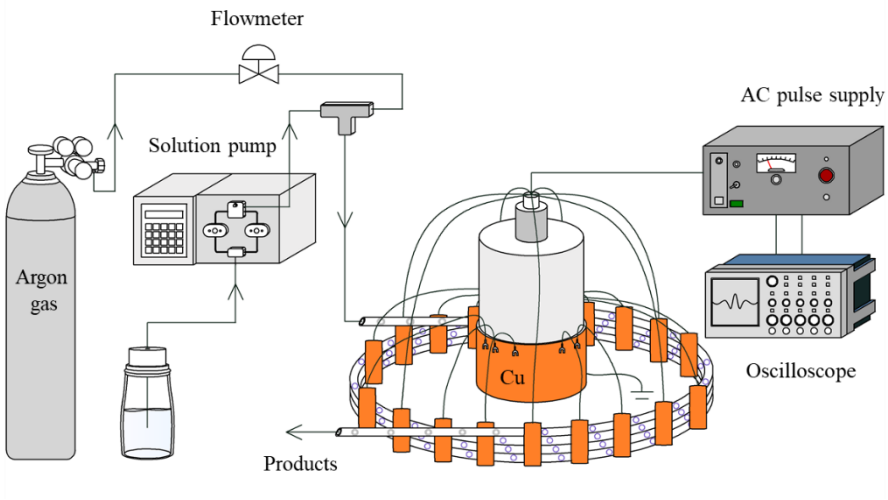

Figure 3.1 Apparatus scheme of synthesizing CeO_2 nanoparticles by atmospheric-pressure pulsed discharge plasma

3.2.3 Analysis methods

The same as mentioned above in Section 2.2.3.

3.3 Results and discussion

3.3.1 Synthesis mechanism of CeO_2 nanoparticles

Figure 3.2 shows the synthesis mechanism of the CeO_2 nanoparticles under atmospheric-pressure pulsed discharge plasma in the slug flow system. When pulsed discharge plasma is introduced in a gas/liquid environment, chemically active species

with oxidizing properties are generated[16]. Firstly, the high-energy electrons accelerated in a high local electric field and ionized argon molecules into an excited argon state, generating initial radicals. The generated radicals then contacted the water interface in the slug flow system and reacted with water molecules. $OH^{\cdot}$ radicals were generated, which show high oxidizing power (E_0 = 2.85V) and are one of the strongest oxygen-based oxidants[17]. Moreover, $OH^{\cdot}$ radicals have a short lifetime in the gas phase and aqueous solutions; therefore, they might directly react with only the species in their immediate surrounding. Next, as shown in Reactions (1) – (5)[18-21], hydroxide ions were generated. And the $OH^{\cdot}$ radicals continued to combine with each other to generate powerful oxidants, such as hydrogen peroxide, oxygen, and ozone[22-24].

$$OH^{\cdot} + e \rightarrow OH^{-} \quad (1)$$

$$OH^{\cdot} + OH^{\cdot} \rightarrow H_2O_2 \quad (2)$$

$$OH^{\cdot} + OH^{\cdot} \rightarrow H_2O + O \quad (3)$$

$$O + OH^{\cdot} \rightarrow O_2 + H^{\cdot} \quad (4)$$

$$O + O_2 \rightarrow O_3 \quad (5)$$

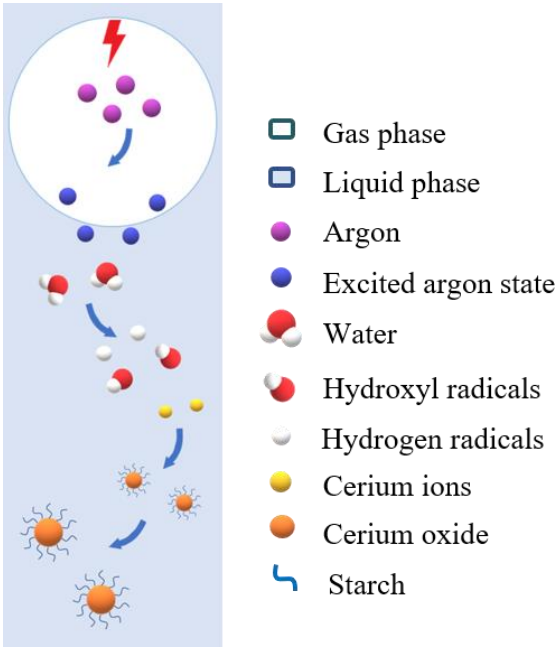

Figure 3.2 The schematic drawing of synthesis mechanism of CeO_2 nanoparticles by atmospheric-pressure pulsed discharge plasma

Due to the generation of oxidizing radicals and molecules by plasma, the Ce^{3+} ions in the feed solution tended to be converted into Ce^{4+} ions[25]. Because Ce^{4+} ions have low basicity and high charge, strong hydrolysis reactions tended to occur[13]. The Ce^{4+} ions combine with H_2O molecules and OH^- ions in the solution to form hydroxide complexes $Ce(OH)_x(H_2O)_y^{(4-x)+}$, which served as the precursors for CeO_2[2, 26], as shown in Reaction (7). The dehydration reaction tended to occur at high local plasma temperatures. H_2O as a polar molecule attracted protons from the OH^- ions, triggering the crystallization of CeO_2[27], according to Reaction (8).

$$Ce^{3+} + H_2O \rightarrow Ce(OH)^{3+} + H^+ + e^- \quad (6)$$

$$Ce^{4+} + xOH^- + yH_2O \rightarrow \left[Ce(OH)_x(H_2O)_y\right]^{(4-x)+} \quad (7)$$

$$\left[Ce(OH)_x(H_2O)_y\right]^{(4-x)+} + H_2O \rightarrow CeO_2 \cdot nH_2O + H_3O^+ \quad (8)$$

where x and y are positive integers.

Instantaneous and homogeneous nucleation occurred in the slug flow system by pulsed discharge plasma. The CeO_2 nanoparticles were generated after a rapid growth process at high excitation temperatures generated by plasma[28]. When starch was added to the feed solution as a stabilizer, the cerium cations in the solution were attracted by the oxygen in the hydroxyl groups of starch[29]. Starch was wrapped around the surface of the CeO_2 nanoparticles to separate the nucleation and growth stages appropriately, which made it possible to control the diameter of the nanoparticles and generate uniform CeO_2 nanoparticles.

3.3.2 Effect of stabilizer on the synthesis of CeO_2 nanoparticles

In the synthesis of nanoparticles, biomaterials with functional groups including –COOH, –OH, and $–NH_2$, are typically used to stabilize and cap metal ions to prevent their aggregation[30]. In this study, starch, which is easily available, economical, and environmentally friendly, was used as stabilizer. It is well known that starch can be used as a stabilizer for the synthesis of different nanoparticles[31-32]. As can be observed from Figure 3.3, the CeO_2 nanoparticles exhibited aggregation in the absence of the stabilizer, not individual spherical nanoparticles. Initially, instantaneous, and homogeneous nucleation occurred in the plasma reactor. In the absence of a stabilizer, the nanoparticle nucleation and growth processes in solutions are not adequately separated, which leads

to the incorporation of the monomers into the previous stable nuclei, resulting in the generation of non-uniform nanoparticles[28]. Therefore, in this study, we added starch as a stabilizer to the feed solution to separate the nucleation and growth processes appropriately to avoid secondary nucleation[33], which was conductive to the formation of uniform CeO_2 nanoparticles. Darroudi et al.[29] proposed that cerium cations in aqueous solutions are attracted by the oxygen of hydroxyl groups in starch, and starch can cover the surface of nanoparticles as a capping agent to prevent their excessive aggregation. Therefore, the diameter of the resulting nanoparticles can be controlled.

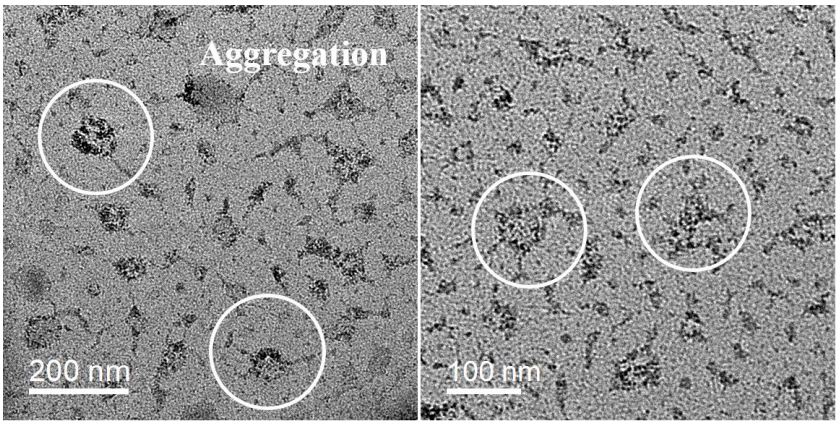

Figure 3.3 TEM images of CeO_2 nanoparticles synthesized without stabilizer

The effect of the stabilizer concentration on the formation of the CeO_2 nanoparticles was investigated. The concentration of starch in the feed solution was varied from 0.1 to 0.4 wt%. As shown in Figure 3.4, with an increase in the starch concentration from 0.1 to 0.4 wt%, the absorbance peaks of the CeO_2 nanoparticles showed similar shapes, and the intensity of the absorption was increased. Ngoc Nhiem Dao et al[34] reported that with the content of CeO_2 nanoparticles increased, UV

absorption intensity was enhanced and UV absorbance peak increased. This indicates that the amount of the CeO_2 nanoparticles formed in the solution increased with an increase in the starch concentration.

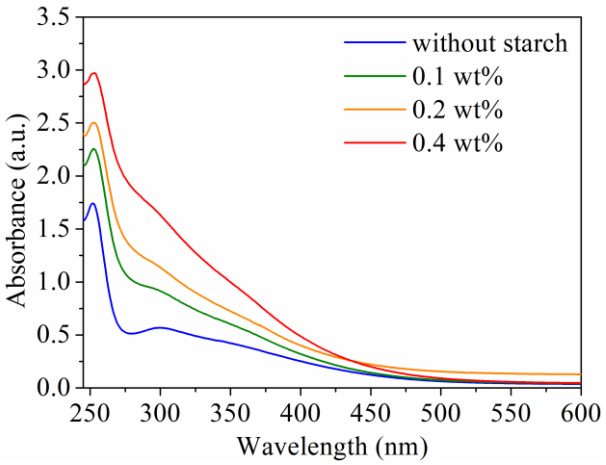

Figure 3.4 UV-vis spectra of CeO_2 nanoparticles synthesized with different concentration of starch

As shown in Figure 3.5, the mean sizes of CeO_2 nanoparticles obtained at the starch concentrations of 0.1, 0.2, and 0.4 wt% were 6.3, 4.9, and 5.1 nm, respectively. This indicates that the starch concentration did not significantly affect the size of the CeO_2 nanoparticles. Thus, higher starch concentrations may be beneficial for stabilizing and capping the CeO_2 nanoparticles. Yamada et al.[35] also obtained high-concentration silver nanoparticles at high starch concentrations by pulsed discharge plasma, and they observed the interaction between –OH functional group in the starch and silver nanoparticles through Fourier transform infrared (FT-IR).

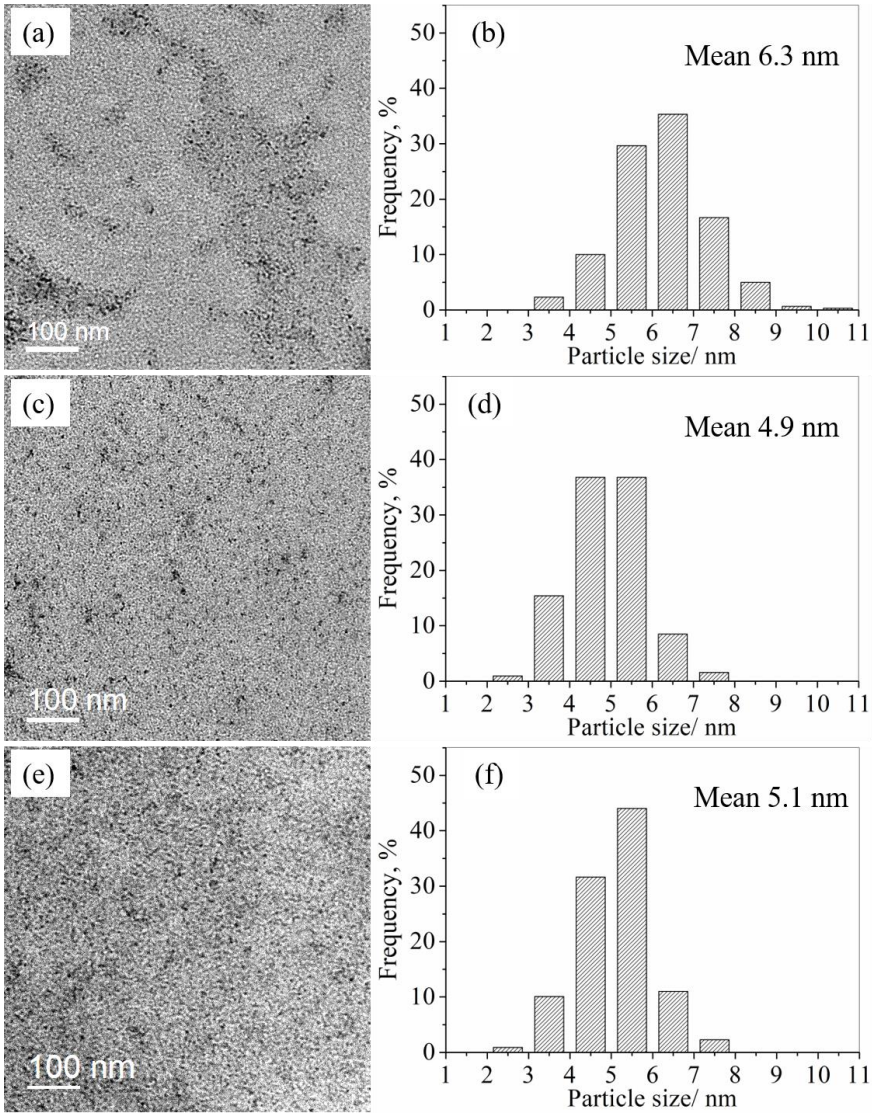

Figure 3.5 TEM images and particle size distributions of CeO_2 nanoparticles with different concentration of starch (a), (b) 0.1 wt%; (c), (d) 0.2 wt%; (e), (f) 0.4 wt%

3.3.3 Effect of slug flow reactor on the synthesis of CeO_2 nanoparticles

In our previous study[35], a straight capillary glass tube with two electrodes was used as the slug flow reactor. As shown in Figure 3.6 a, the length of the glass tube was 0.12 m and the distance between the two copper electrodes was approximately 25 mm. CeO_2

nanoparticles could be synthesized by pulsed discharge plasma in the system, however, the amount of the CeO_2 nanoparticles generated was low. Therefore, in this study, we increased the length of the reactor tube and the number of electrodes to prolong the reaction residence time to increase the CeO_2 nanoparticles yield. Yamada et al.[36] used a circular capillary glass tube coil as the slug flow reactor for decolorizing methylene blue and achieved high decolorization efficiency. As shown in Figure 3.6 b, fifteen copper electrodes, including five high-voltage electrodes and ten ground electrodes, were arranged on a circular capillary glass tube coil with a length of 2.0 m. The distance between the two adjacent electrodes was approximately 25 mm. The residence time of the plasma state bubbles increased approximately from 3 s to 3 min with the use of this assembly.

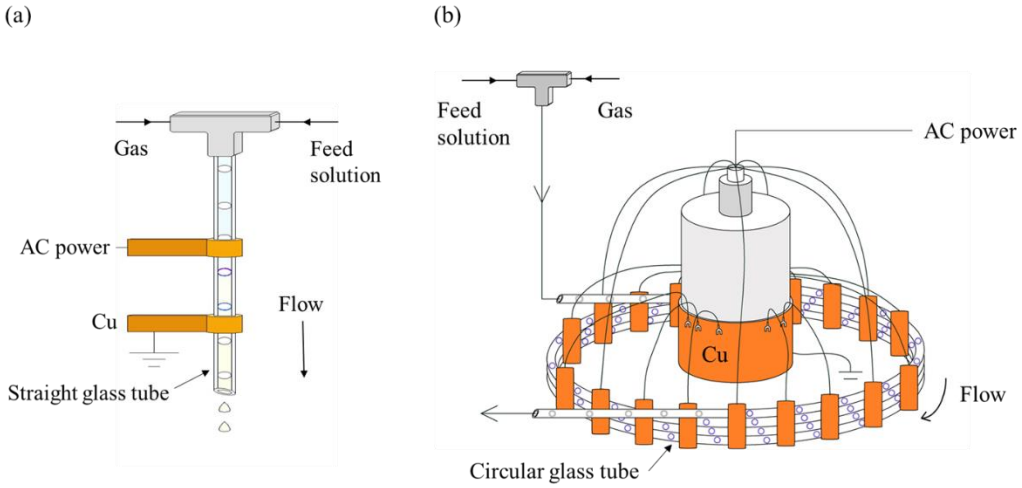

Figure 3.6 Slug flow reactor (a) straight capillary glass tube; (b) circular capillary glass tube coil

Impact ionization, which occurs in a high local electric field, is the main ionization

mechanism in electric discharges[37]. In this process, electrons are accelerated and ionize gas molecules or atoms to generate more electrons. The use of the circular capillary glass tube coil as the slug flow reactor increases the number of plasma production sites, and the number of energetic electrons increases with an increase in the input energy. More electrons impact the gas molecules, which leads to the generation of more reactive species, including $OH\cdot$, H_2O_2, and O_3 species[35, 38]. Nanoparticles are obtained after the nucleation and growth processes[28]. With an increase in the number of electrodes and residence time, a large number of Ce^{3+} ions get involved in the oxidation reaction to produce hydroxide complexes[2]. For cold plasma, most of the coupled electrical energy is primarily channeled to the electron component to produce energetic electrons[39]. Therefore, electron temperature is much higher than room temperature[40-41]. CeO_2 nanoparticle nuclei are generated via dehydration from the hydroxide complexes at the high local plasma temperatures[22]. An increase in the nucleation frequency results in an increase in the number of the nuclei and CeO_2 nanoparticles formed.

Figure 3.7 shows the UV-vis spectra of the CeO_2 nanoparticle-containing solutions obtained using different slug flow reactors. The CeO_2 nanoparticles showed significant UV absorption peaks at approximately 250 and 300 nm. The intensity of these peaks increased when a circular capillary glass tube coil was used as the slug flow reactor, indicating an increase in the number of the CeO_2 nanoparticles formed.

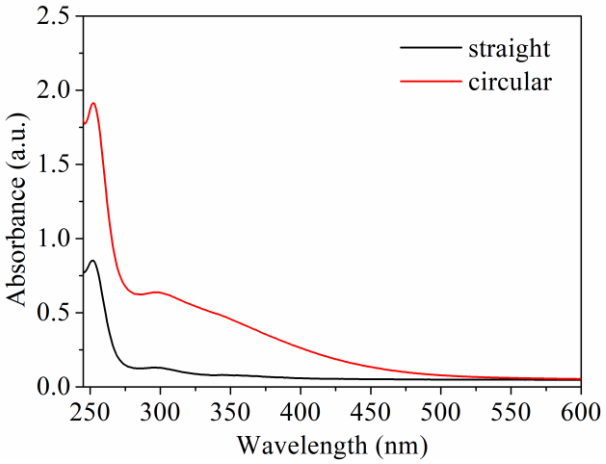

Figure 3.7 UV-vis spectra of solution products synthesized by the different slug flow reactors

The particle size distributions of the CeO_2 nanoparticles synthesized in the two reactors were also analyzed. As shown in Figure 3.5 b, the mean size of the CeO_2 nanoparticles synthesized in the circular capillary glass tube coil was approximately 6.3 nm. And the mean size synthesized in the straight capillary tube was approximately 3.4 nm (Figure 2.5 c). When the circular capillary glass tube coil was used as the reactor, the nucleation frequency and number of nuclei increased. The time required for the growth of the nuclei increased with an increase in the residence time, which resulted in an increase in the size of the CeO_2 nanoparticles. Furthermore, the aggregation of the nuclei resulted in the generation of larger nanoparticles.

3.3.4 Effect of cerium source on the structure of cerium oxide nanoparticles

As mentioned above, CeO_2 (IV) nanoparticles were obtained when cerium nitrate (III) was used as a cerium source. In order to attempt to synthesize Ce_2O_3 nanoparticles,

cerium source was changed, and the effect of cerium source on structure of cerium oxide nanoparticles was also investigated. Ammonium cerium nitrate (IV) of 1 mmol/L without a stabilizer was used as the feed solution firstly. A yellow solution was obtained after plasma treatment (Figure 3.8), and it was characterized by TEM, as shown in Figure 3.9. Many column crystals were generated and aggregated together. Nanoparticles were difficult to be observed.

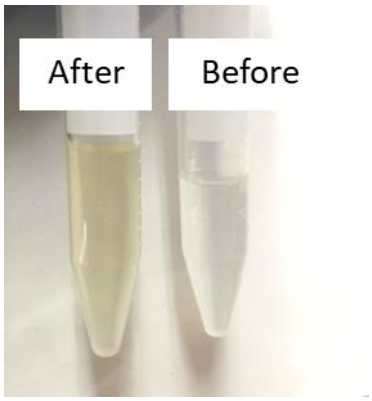

Figure 3.8 Photographs of product after plasma treatment and feed solution

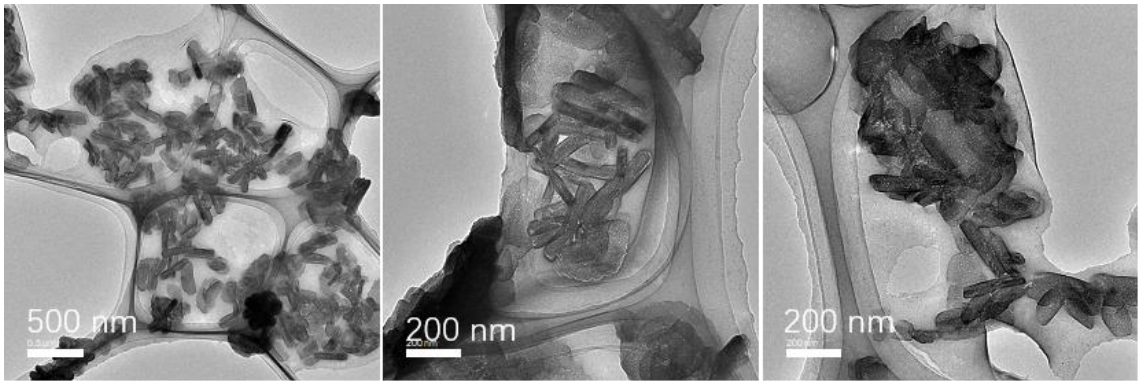

Figure 3.9 TEM images of the product synthesized using ammonium cerium nitrate without a stabilizer

Hence starch of 0.1 wt% was added into the feed solution as a stabilizer, and product after treatment was characterized by TEM. As shown in Figure 3.10, irregular crystals were also generated. And spherical nanoparticles could be observed, the mean size of the nanoparticles was measured to be 3.98 nm. Elemental distributions of the irregular crystals were analyzed by EDS. As shown in Figure 3.11, nitrogen and oxygen were detected in the elemental maps, consistent with the position of irregular crystal in the grey TEM images. Metallic cerium was detected as tiny particles and inconsistent with the position of the crystal. It suggests that the irregular crystal is not cerium oxide and may be the result of nitrogen aggregation. Therefore, starch may be not a suitable stabilizer to synthesize cerium oxide nanoparticles for ammonium cerium nitrate.

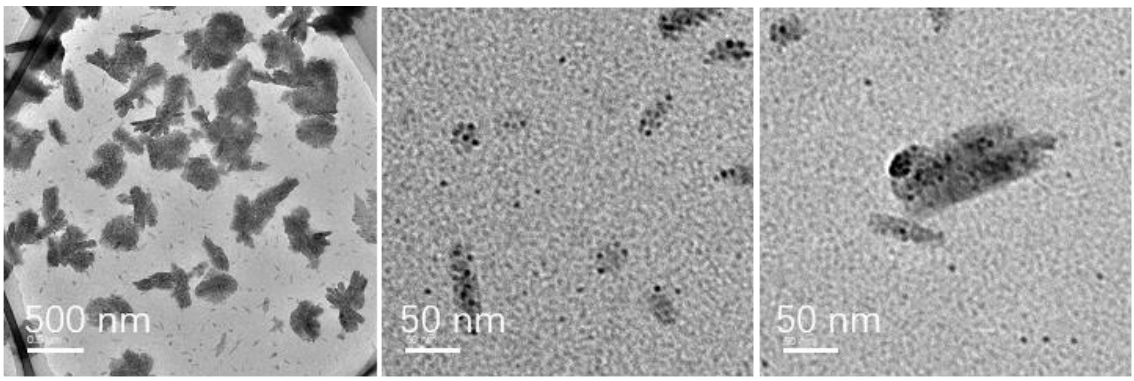

Figure 3.10 TEM images of the product synthesized using ammonium cerium nitrate with starch as stabilizer

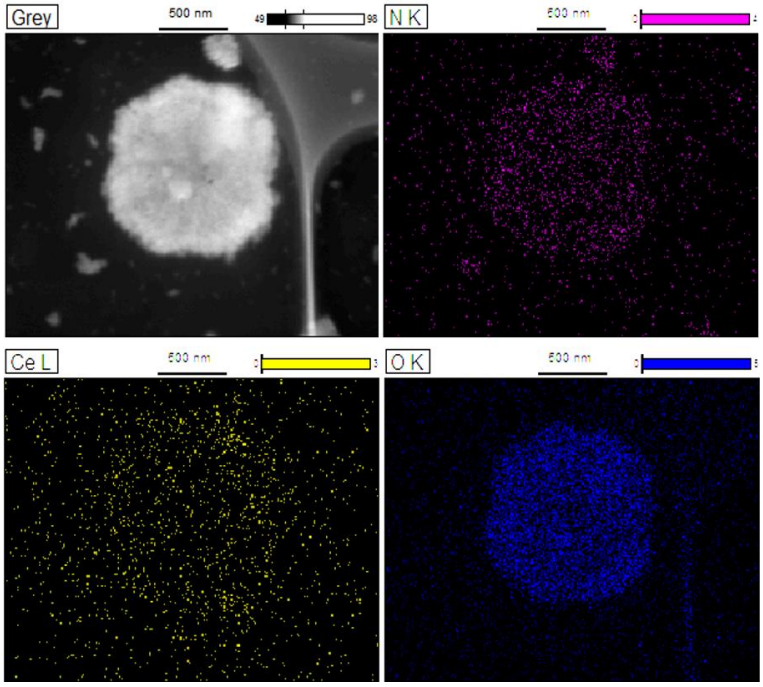

Figure 3.11 EDS maps of the product synthesized using ammonium cerium nitrate with starch as stabilizer

Proline is an amino acid with the functional group –COOH. It has shown effective stability in controlling the aggregation of intravenous immunoglobulin[42]. And it was also reported that proline as a ligand enhanced activity and selectivity of Pt nanoparticles in heterogeneous catalysis[43]. Proline of 0.1 wt% was added as another stabilizer into the feed solution, and product after plasma treatment was characterized by TEM. As shown in Figure 3.12, spherical nanoparticles were observed without the generation of the irregular crystals. The mean size of the nanoparticles was measured to be 3.46 nm. Figure 3.13 shows the elemental maps and spectrum of the nanoparticles. The peaks corresponding to cerium could be observed in the spectrum. Elements of cerium and oxygen were also detected in the elemental maps, indicating cerium oxide nanoparticles were generated using ammonium cerium nitrate with proline as a

stabilizer.

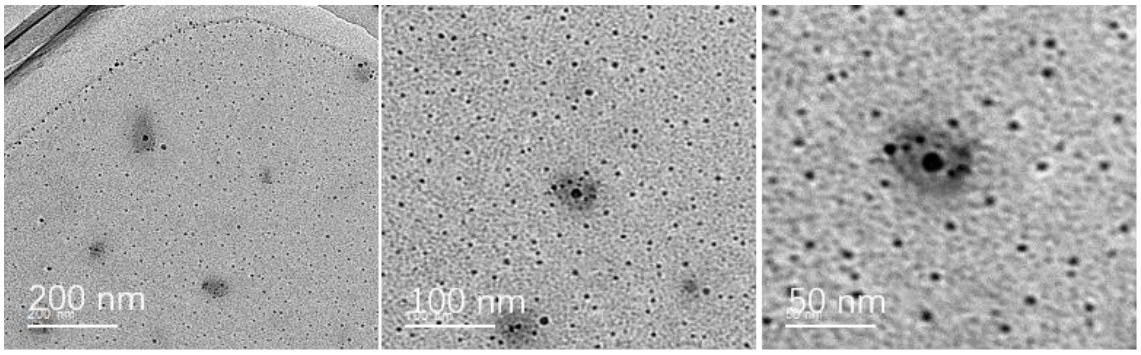

Figure 3.12 TEM images of the product synthesized using ammonium cerium nitrate with proline as stabilizer

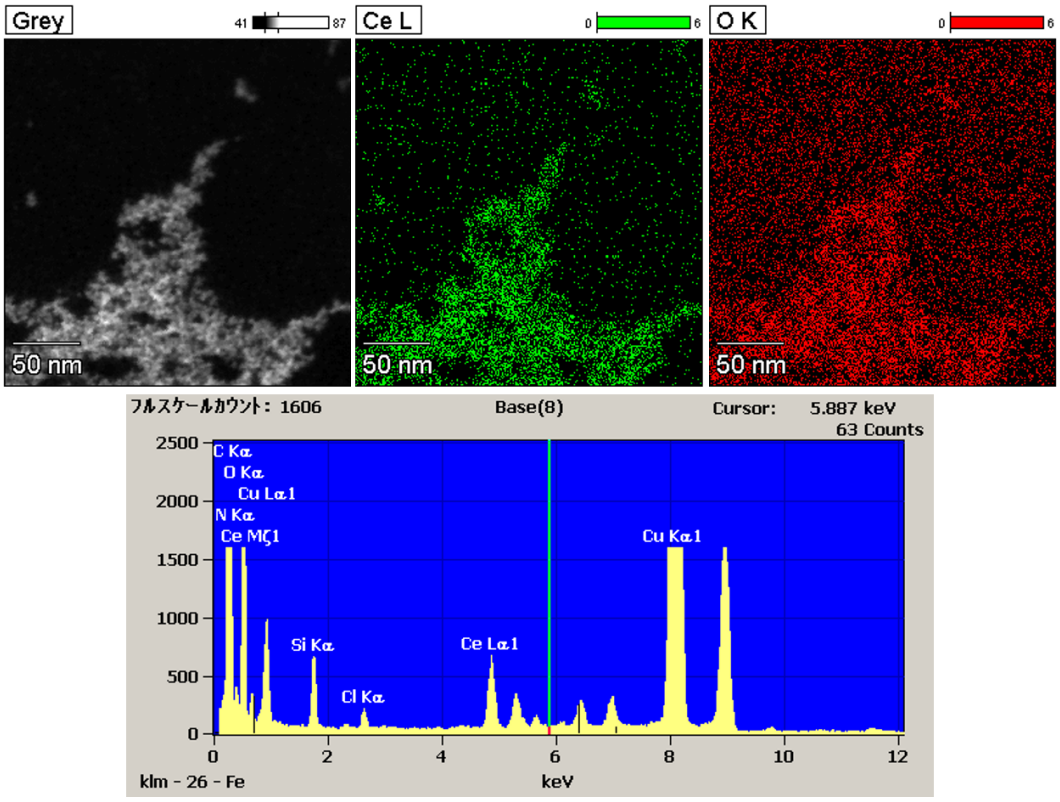

Figure 3.13 EDS maps and spectrum of cerium oxide nanoparticles synthesized using ammonium cerium nitrate with proline as stabilizer

The crystal structure of cerium oxide nanoparticles was analyzed by HRTEM

images and SAED patterns. The lattice fringes in the HRTEM images (Figure 3.14 a) showed a spacing of 0.29 nm due to (011) planes and a spacing of 0.33 nm due to the (100) planes of hexagonal Ce_2O_3[6]. The spacing of 0.31 nm due to (111) planes of cubic CeO_2 was also shown from the lattice fringes. As shown in Figure 3.14 b, the SAED pattern of the nanoparticles showed the rings corresponding to the (011) planes of Ce_2O_3. The results indicated the existence of both hexagonal Ce_2O_3 and cubic CeO_2 in the product. As mentioned before, various reactive species were generated during the plasma process, including $OH^{\cdot}$ radicals and $H^{\cdot}$ radicals[44]. The $H^{\cdot}$ radical is a powerful reducing agent (E_0 = -2.3V)[45]. Hence, a part of tetravalent cerium ions in the feed solution might tend to be reduced into trivalent cerium ions, generating the hydroxide complexes served as the precursors of Ce_2O_3. During the plasma reactions, electron collisions with molecules or atoms generate highly reactive growth precursors, leading to the largely irreversible nanoparticle growth process, allowing the generation of Ce_2O_3 nanoparticles[46].

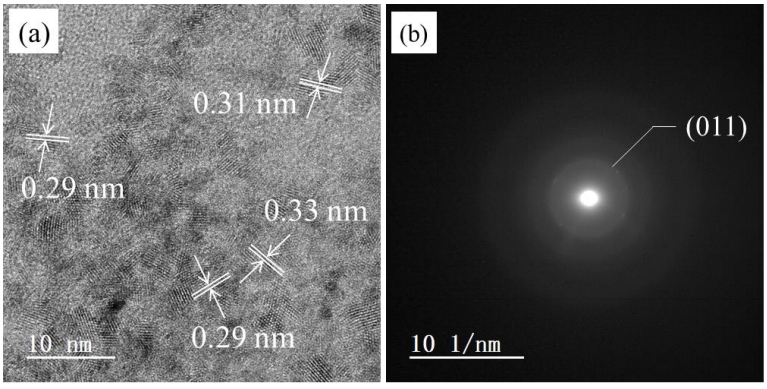

Figure 3.14 (a) HRTEM image and (b) SAED pattern of cerium oxide nanoparticles synthesized using ammonium cerium nitrate with proline as stabilizer

3.4 Conclusion

In this study, CeO_2 and Ce_2O_3 nanoparticles were synthesized in a slug flow system using atmospheric-pressure pulsed discharge plasma. In the process of generating CeO_2 nanoparticles, radical species were produced and reacted with cerium ions (III) in the feed solution, resulting in an instantaneous and homogeneous nucleation and rapid growth of the nanoparticles. The effects of the process factors on the synthesis of the CeO_2 nanoparticles were discussed. The main findings of the study are as follows:

1) The slug flow system provided a continuous reaction field in the gas/liquid plasma environment, which was beneficial for the synthesis of uniform nanoparticles. When a circular capillary glass tube coil was used as the slug flow reactor and $Ce(NO_3)_3$ with 0.1 wt% starch was used as the feed solution, uniform CeO_2 nanoparticles with mean size of approximately 6.3 nm were obtained.

2) Starch was added as a stabilizer to separate the nucleation and growth processes and prevent the aggregation of the resulting nanoparticles. With an increase in the starch concentration from 0.1 to 0.4 wt%, the amount of the CeO_2 nanoparticles increased and their size distribution did not change significantly.

3) The difference between the straight tube and circular glass tube coil as the slug flow reactors was discussed. When the circular capillary glass tube coil was used as the reactor, the electrodes number was increased and the residence time was prolonged. The concentration of CeO_2 nanoparticles increased and mean size also increased from 3.4 to 6.3 nm compared to the case using straight tube as the slug flow reactor.

4) It is difficult to synthesize Ce_2O_3 nanoparticles using traditional methods. When

using ammonium cerium (IV) nitrate as the feed solution in the gas/liquid plasma system, Ce_2O_3 nanoparticles were observed to be generated, which might be due to the existence of $H^{\cdot}$ radicals and irreversible nanoparticle growth process during the plasma reactions.

References

1. Zhou, Y. C.; Rahaman, M. N., Hydrothermal synthesis and sintering of ultrafine CeO~ 2 powders. *Journal of materials research* **1993,** *8* (5), 1680-1686.
2. Hirano, M.; Kato, E., Hydrothermal Synthesis of Cerium(IV) Oxide. *Journal of the American Ceramic Society* **1996,** *79* (3), 777-780.
3. Babitha, K.; Sreedevi, A.; Priyanka, K.; Sabu, B.; Varghese, T., Structural characterization and optical studies of CeO2 nanoparticles synthesized by chemical precipitation. *Indian Journal of Pure & Applied Physics (IJPAP)* **2015,** *53* (9), 596-603.
4. Su, Y.; Yang, W.; Sun, W.; Li, Q.; Shang, J. K., Synthesis of mesoporous cerium–zirconium binary oxide nanoadsorbents by a solvothermal process and their effective adsorption of phosphate from water. *Chemical Engineering Journal* **2015,** *268*, 270-279.
5. Hirano, M.; Fukuda, Y.; Iwata, H.; Hotta, Y.; Inagaki, M., Preparation and spherical agglomeration of crystalline cerium (IV) oxide nanoparticles by thermal hydrolysis. *Journal of the American Ceramic Society* **2000,** *83* (5), 1287-1289.
6. Verma, R.; Samdarshi, S.; Bojja, S.; Paul, S.; Choudhury, B., A novel thermophotocatalyst of mixed-phase cerium oxide (CeO2/Ce2O3) homocomposite nanostructure: Role of interface and oxygen vacancies. *Solar Energy Materials and Solar Cells* **2015,** *141*, 414-422.
7. Wang, C.; Wang, H. L.; Gao, D. W.; Zhao, Z. K. In *Amorphous NiCoPt/Ce2O3 Nanoparticles as Highly Efficient Catalyst for Hydrogen Generation from Hydrous Hydrazine*, Materials Science Forum, Trans Tech Publ: 2017; pp 1862-1870.
8. Karthikeyan, M., Production of biodiesel from Cordiamyxa bio-oil using BaMoO4-Ce2O3 nanoparticles as an alternative fuel for diesel engine. *Materials Letters* **2019,** *243*, 199-201.
9. Hussain, M. M.; Rahman, M. M.; Asiri, A. M., Efficient 2-nitrophenol chemical sensor development based on Ce2O3 nanoparticles decorated CNT nanocomposites for environmental safety. *PLoS One* **2016,** *11* (12), e0166265.
10. Nadaroglu, H.; Onem, H.; Gungor, A. A., Green synthesis of Ce 2 O 3 NPs and determination of its antioxidant activity. *Iet Nanobiotechnology* **2017,** *11* (4), 411-419.
11. Hassan, M. S.; Amna, T.; Al-Deyab, S. S.; Kim, H.-C.; Oh, T.-H.; Khil, M.-S., Toxicity of Ce2O3/TiO2 composite nanofibers against S. aureus and S. typhimurium: A novel electrospun material for disinfection of food pathogens. *Colloids and Surfaces A: Physicochemical and Engineering Aspects* **2012,** *415*, 268-273.
12. Onwudiwe, D. C.; Phadi, B. M.; Oyewo, O. A., Ce2O3/BiVO4 Embedded in rGO as Photocatalyst for the Degradation of Methyl Orange under Visible Light Irradiation. *J* **2021,** *4* (2), 154-168.
13. Wang, H.; Zhu, J.-J.; Zhu, J.-M.; Liao, X.-H.; Xu, S.; Ding, T.; Chen, H.-Y., Preparation of nanocrystalline ceria particles by sonochemical and microwave assisted heating methods. *Physical Chemistry Chemical Physics* **2002,** *4* (15), 3794-3799.
14. Lin, L.; Ma, X.; Li, S.; Wouters, M.; Hessel, V., Plasma-electrochemical synthesis of europium doped cerium oxide nanoparticles. *Frontiers of Chemical Science and Engineering* **2019,** *13* (3), 501-510.

15. Ma, W.; Mashimo, T.; Tamura, S.; Tokuda, M.; Yoda, S.; Tsushida, M.; Koinuma, M.; Kubota, A.; Isobe, H.; Yoshiasa, A., Cerium oxide (CeO2-x) nanoparticles with high Ce3+ proportion synthesized by pulsed plasma in liquid. *Ceramics International* **2020,** *46* (17), 26502-26510.
16. Yamada, M.; Wahyudiono; Machmudah, S.; Kanda, H.; Zhao, Y.; Goto, M., Atmospheric-Pressure Pulsed Discharge Plasma in a Slug Flow Reactor System for the Synthesis of Gold Nanoparticles. *ACS omega* **2020,** *5* (28), 17679-17685.
17. Locke, B. R.; Lukes, P.; Brisset, J.-L., Elementary Chemical and Physical Phenomena in Electrical Discharge Plasma in Gas–Liquid Environments and in Liquids. In *Plasma Chemistry and Catalysis in Gases and Liquids*, pp 185-241.
18. Joshi, R. P.; Thagard, S. M., Streamer-Like Electrical Discharges in Water: Part II. Environmental Applications. *Plasma Chemistry and Plasma Processing* **2013,** *33* (1), 17-49.
19. Locke, B. R.; Sato, M.; Sunka, P.; Hoffmann, M. R.; Chang, J. S., Electrohydraulic Discharge and Nonthermal Plasma for Water Treatment. *Industrial & Engineering Chemistry Research* **2006,** *45* (3), 882-905.
20. Wang, K.; Tan, H.; Lin, Y.; Diono, W.; Zhao, Y.; Goto, M., Direct current gas–liquid phase pulsed plasma polymerization of polypyrrole under atmospheric pressure. *Plasma Processes and Polymers* **2020**, e2000186.
21. Ognier, S.; Iya-Sou, D.; Fourmond, C.; Cavadias, S., Analysis of mechanisms at the plasma–liquid interface in a gas–liquid discharge reactor used for treatment of polluted water. *Plasma Chemistry and Plasma Processing* **2009,** *29* (4), 261-273.
22. Chu, P. K.; Lu, X., Low temperature plasma technology: methods and applications. CRC Press: 2013.
23. Sun, B.; Aye, N. N.; Gao, Z.; Lv, D.; Zhu, X.; Sato, M., Characteristics of gas-liquid pulsed discharge plasma reactor and dye decoloration efficiency. *Journal of Environmental Sciences* **2012,** *24* (5), 840-845.
24. Lu, N.; Li, J.; Wu, Y.; Masayuki, S., Treatment of Dye Wastewater by Using a Hybrid Gas/Liquid Pulsed Discharge Plasma Reactor. *Plasma Science and Technology* **2012,** *14* (2), 162-166.
25. Calvache-Muñoz, J.; Prado, F. A.; Rodríguez-Páez, J. E., Cerium oxide nanoparticles: Synthesis, characterization and tentative mechanism of particle formation. *Colloids and Surfaces A: Physicochemical and Engineering Aspects* **2017,** *529*, 146-159.
26. Chen, P. L.; Chen, I. W., Reactive cerium (IV) oxide powders by the homogeneous precipitation method. *Journal of the American Ceramic Society* **1993,** *76* (6), 1577-1583.
27. Xin, Y.; Yang, X.; Jiang, P.; Zhang, Z.; Wang, Z.; Zhang, Y., Synthesis of CeO_2-Based Quantum Dots through a Polyol-Hydrolysis Method for Fuel-Borne Catalysts. *ChemCatChem* **2011,** *3* (11), 1772-1778.
28. Thanh, N. T. K.; Maclean, N.; Mahiddine, S., Mechanisms of Nucleation and Growth of Nanoparticles in Solution. *Chemical Reviews* **2014,** *114* (15), 7610-7630.
29. Darroudi, M.; Sarani, M.; Oskuee, R. K.; Zak, A. K.; Hosseini, H. A.; Gholami, L., Green synthesis and evaluation of metabolic activity of starch mediated nanoceria.

Ceramics International **2014,** *40* (1), 2041-2045.
30. Charbgoo, F.; Ahmad, M. B.; Darroudi, M., Cerium oxide nanoparticles: green synthesis and biological applications. *International journal of nanomedicine* **2017,** *12*, 1401.
31. Zamiri, R.; Azmi, B.; Darroudi, M.; Sadrolhosseini, A. R.; Husin, M.; Zaidan, A.; Mahdi, M., Preparation of starch stabilized silver nanoparticles with spatial self-phase modulation properties by laser ablation technique. *Applied Physics A* **2011,** *102* (1), 189-194.
32. Zak, A. K.; Majid, W. A.; Mahmoudian, M.; Darroudi, M.; Yousefi, R., Starch-stabilized synthesis of ZnO nanopowders at low temperature and optical properties study. *Advanced Powder Technology* **2013,** *24* (3), 618-624.
33. Varanda, L. C.; Souza, C. G. S.; Moraes, D. A.; Neves, H. R.; Souza Junior, J. B.; Silva, M. F.; Bini, R. A.; Albers, R. F.; Silva, T. L.; Beck Junior, W., Size and shape-controlled nanomaterials based on modified polyol and thermal decomposition approaches. A brief review. *Anais da Academia Brasileira de Ciências* **2019,** *91*.
34. Dao, N. N.; Dai Luu, M.; Nguyen, Q. K.; Kim, B. S., UV absorption by cerium oxide nanoparticles/epoxy composite thin films. *Advances in Natural Sciences: Nanoscience and Nanotechnology* **2011,** *2* (4), 045013.
35. Yamada, M.; Takahashi, S.; Wahyudiono; Takada, N.; Kanda, H.; Goto, M., Synthesis of silver nanoparticles by atmospheric-pressure pulsed discharge plasma in a slug flow system. *Japanese Journal of Applied Physics* **2019,** *58* (1), 016001.
36. Yamada, M.; Machmudah, S.; Kanda, H.; Goto, M., Nonthermal Atmospheric Pressure Plasma for Methylene Blue Dye Decolorization by Using Slug Flow Reactor System. *Plasma Chemistry and Plasma Processing* **2020**, 1-16.
37. Nijdam, S.; van Veldhuizen, E.; Bruggeman, P.; Ebert, U., An Introduction to Nonequilibrium Plasmas at Atmospheric Pressure. *Plasma Chemistry and Catalysis in Gases and Liquids*, Wiley-VCH Verlag GmbH & Co. KGaA, 2012; pp 1-44.
38. Diono, W.; Mano, K.; Hayashi, Y.; Yamada, M.; Takahashi, S.; Takada, N.; Kanda, H.; Goto, M., Atmospheric-pressure pulsed discharge plasma in capillary slug flow system for dye decomposition. *Chemical Engineering and Processing - Process Intensification* **2018,** *135*.
39. Nehra, V.; Kumar, A.; Dwivedi, H., Atmospheric non-thermal plasma sources. *International Journal of Engineering* **2008,** *2* (1), 53-68.
40. Tabares, F. L.; Junkar, I., Cold Plasma Systems and their Application in Surface Treatments for Medicine. *Molecules* **2021,** *26* (7), 1903.
41. Tanner, S. D., Characterization of ionization and matrix suppression in inductively coupled 'cold'plasma mass spectrometry. *Journal of Analytical Atomic Spectrometry* **1995,** *10* (11), 905-921.
42. Bolli, R.; Woodtli, K.; Bärtschi, M.; Höfferer, L.; Lerch, P., L-Proline reduces IgG dimer content and enhances the stability of intravenous immunoglobulin (IVIG) solutions. *Biologicals* **2010,** *38* (1), 150-157.
43. Schrader, I.; Warneke, J.; Backenköhler, J.; Kunz, S., Functionalization of Platinum Nanoparticles with l-Proline: Simultaneous Enhancements of Catalytic Activity and Selectivity. *Journal of the American Chemical Society* **2015,** *137* (2), 905-912.

44. Hawtof, R.; Ghosh, S.; Guarr, E.; Xu, C.; Mohan Sankaran, R.; Renner, J. N., Catalyst-free, highly selective synthesis of ammonia from nitrogen and water by a plasma electrolytic system. *Science advances* **2019,** *5* (1), eaat5778.
45. Locke, B. R.; Lukes, P.; Brisset, J.-L., Elementary chemical and physical phenomena in electrical discharge plasma in gas-liquid environments and in liquids. *Plasma chemistry and catalysis in gases and liquids*; Wiley-VCH Verlag GmbH & Co. KGaA, **2012**; pp 185-241
46. Kortshagen, U. R.; Sankaran, R. M.; Pereira, R. N.; Girshick, S. L.; Wu, J. J.; Aydil, E. S., Nonthermal Plasma Synthesis of Nanocrystals: Fundamental Principles, Materials, and Applications. *Chemical Reviews* **2016,** *116* (18), 11061-11127.

Chapter 4. Gas/liquid pulsed discharge plasma in a slug flow reactor under pressurized argon

4.1 Introduction

4.1.1 Plasma system under pressurized conditions

Currently researches on plasma under high-pressure conditions are relatively rare, but meaningful results have been obtained in the reaction field. Sasaki. et al.[1] found that in microwave helium plasmas, electron temperature increased with the discharge pressure, one of reasons for which is the production of electrons with medium energy through heavy particle collisions at the high gas pressure. Hayashi. et al.[2] reported that after applying pulsed discharge plasma in a gas-liquid medium with a copper rod as an electrode, carbon solid materials were only produced under high-pressure conditions. Wahyudiono et al.[3] also reported that the conversation rate of pyrrole increased with increasing reaction pressure. This may originate to the higher voltage required for the gas breakdown under higher-pressure conditions, which led to higher energy on plasma generation.

As shown in Paschen curves[4] in Figure 4.1, with a constant gap length, as the pressure continues to increase above a specific value, required breakdown voltage also increases. Theoretically, the density of gas molecules or atoms increases with pressure increasing, enhancing the collisions between high-energy electrons and gas molecules or atmos. Collisional energy loss increases, and increasing input voltage is required to

provide sufficient energy to ionize gas molecules or atoms. Accordingly, the amount of generated reactive species is expected to be increased. In addition, as the pressure increasing, dissolution of gas and active species in the liquid phase also increases, beneficial for the subsequent reactions in the solution. Therefore, it is worth investigating the gas/liquid plasma system under high-pressure conditions. But new challenges have also arisen, as higher voltage is required for gas breakdown and there are difficulties to maintain the plasma under pressurized conditions.

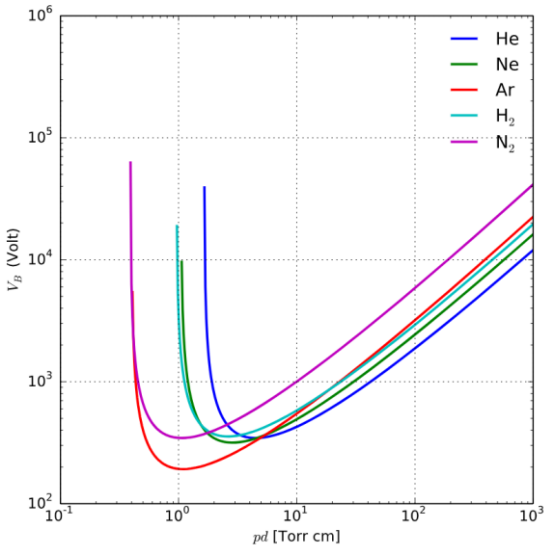

Figure 4.1 Paschen curves obtained for helium, neon, argon, hydrogen and nitrogen[4]

4.1.2 Motivation and purpose of this work

In this study, in order to further investigate the slug flow system using pulsed discharge plasma, it is first utilized under pressurized argon. The insight of chemical

properties on this system is studied under different system pressure. Reactive species generated in the system by pulsed discharge plasma are qualitatively and quantitatively analyzed, and the input energy is also calculated. The effect of pressure on the system is studied.

4.2 Experimental procedure

4.2.1 Materials

Sodium chloride (NaCl) (Product No. 191-01665), potassium iodide (KI) (Product No. 168-03975), sodium thiosulfate pentahydrate ($Na_2S_2SO_3$•$5H_2O$) (Product No. 197-03585), starch (Product No.191-03985) and distilled water (Product No. 049-16787) were purchased from Wako Pure Chemical Industries, Ltd., Osaka, Japan. Argon (purity > 99.99%) was purchased from Sogo Kariya Sanso, Inc., Nagoya, Japan. All the chemicals used in this study were used as received without further purification.

4.2.2 Experimental methods

Schematic of the slug flow system using gas/liquid plasma under higher-pressure conditions is shown as Figure 4.2. A straight capillary glass tube (300 mm×2.0 mm i.d., Fujirika Kogyo Co., FPT-300, Osaka, Japan) was used as the slug flow reactor. Bubbles and gas/liquid interfaces were generated by flowing gas and feed solution through a T-type junction (SS-200-3, Swagelok) simultaneously. Flow rates of gas and feed solution

were controlled by a metering valve and a high-performance liquid chromatography solution pump (LC-10AD, Shimadzu Co., Kyoto, Japan), respectively. Residence time of plasma-state bubbles was approximately 20 seconds. Copper (Cu) sheets of 1 cm width were attached to outer capillary glass tube as electrodes. Seven electrodes including 4 high-voltage electrodes and 3 ground electrodes were arranged. Distance between the adjacent electrodes was approximately 25 mm. A high voltage of 11 kV was introduced into the system by an AC pulse supply (TE-HVP1510K300-NP, Tamaoki Electronics Co., Ltd., Kawaguchi, Japan). The flow rates of the feed solution and gas were approximately 1.5 and 1.3 ml/min. As the higher pressure, the gas density increases in proportion to the pressure.

Similar to the system under atmospheric pressure, components controlling and observing system pressure were added. System pressure was controlled at from 0.1 MPa (atmosphere) to 0.4 MPa by a back pressure valve, which could be observed by a pressure meter. Feed solution flowed into the system by a solution pump, while argon gas was introduced from a stop valve. Inlet pressure was controlled by a cylinder pressure valve, and flow rate of the gas was adjusted by a metering valve.

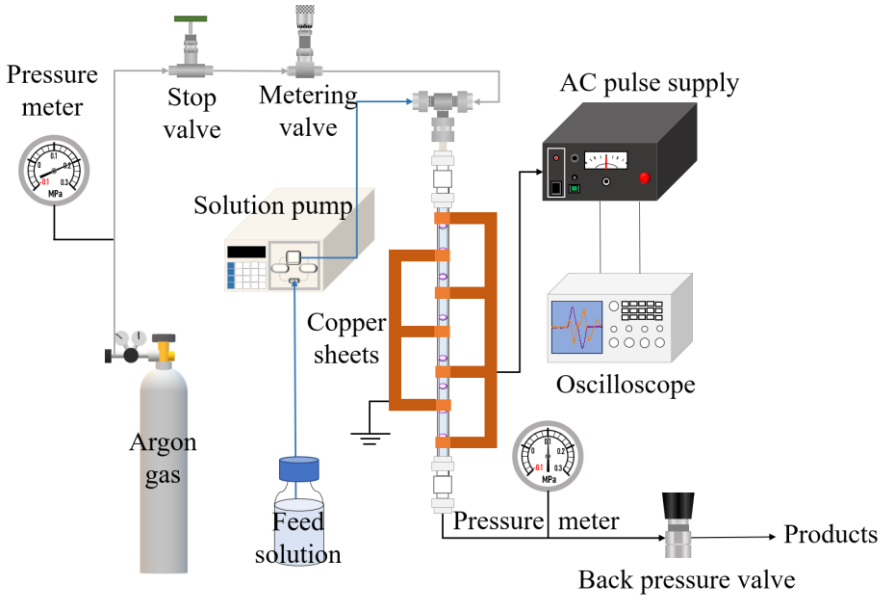

Figure 4.2 Apparatus of slug flow system with pulsed discharge plasma under pressurized condition

4.2.3 Analysis methods

Cold plasmas are characterized by the fact that temperature of heavy species is closed to room temperature[5], which is one of its advantages. Hence, the thermal temperature of the slug flow plasma reaction field under high pressure was measured using a compact thermal imaging camera (FLIR C3-X, Teledyne FLIR LLC, Wilsonville, USA).

The optical emission spectra (OES) were measured approximately 1 cm above the middle of capillary glass tube. Spectra were observed as plasma-state bubbles flowed through the detector. Water and methylene blue aqueous solution with NaCl providing conductivity were used as feed solution under 0.1 and 0.3 MPa, respectively. To measure the energy input, the voltage and current of the system were observed using an

oscilloscope (TDS2024C, Tektronix Inc., OR, USA). A high-resolution optical fiber spectrometer linked to a computer running OPwave+ was also used, and HR4000 (Ocean Insight, Tokyo, Japan) was used for the optical emission spectral analysis.

Concentration of total oxidation species is determined by iodimetry. The mixture of 1.0 wt% potassium iodide (KI) and 0.1 wt% starch aqueous solution was used as feed solution. After plasma treatment, iodine ions in the solution were oxidized into iodine, as shown in the following reactions, which turned brown when encountering starch[6]. Approximately 15 g of the sample was collected and weighed. Sodium thiosulfate ($Na_2S_2O_3$) aqueous solution of 0.01 mmol/L was added into the sample through a burette. Iodine reacted with sodium thiosulfate and the brown color gradually disappeared. Titrations finished until color didn't appear in 30 s, and the weight of $Na_2S_2O_3$ aqueous solution was recorded. The amount of total oxidation species is same with that of $Na_2S_2O_3$, which could be calculated by Equation 4-1. Titrations were repeated at least five times and averaged.

$$Concentration\ of\ total\ oxidation\ species = \frac{m(\mathrm{Na_2S_2O_3}) \times \omega(\mathrm{Na_2S_2O_3})}{M(\mathrm{Na_2S_2O_3}) \times V(sample)} \quad (4\text{-}1)$$

where $m(Na_2S_2O_3)$ is weight of $Na_2S_2O_3$ aqueous solution used in titration;

$\omega(Na_2S_2O_3)$ is mass fraction of $Na_2S_2O_3 \cdot 5H_2O$ in the aqueous solution;

$M(Na_2S_2O_3)$ is molar mass of $Na_2S_2O_3 \cdot 5H_2O$, with a value of 248;

V(sample) is volume of sample.

$$2I^- \xrightarrow{\text{oxidation}} I_2 + 2e^-$$

$$2Na_2S_2O_3 + I_2 = Na_2S_4O_6 + 2NaI$$

4.3 Results and discussion

4.3.1 Thermal images of the slug flow plasma system

Thermal images and visible images of the slug flow system under 0.4 MPa were shown as Figure 4.3, showing the highest temperature of approximately 40℃. It indicates that the system pressure was a little higher than room temperature under a higher-pressure condition, which was acceptably cold.

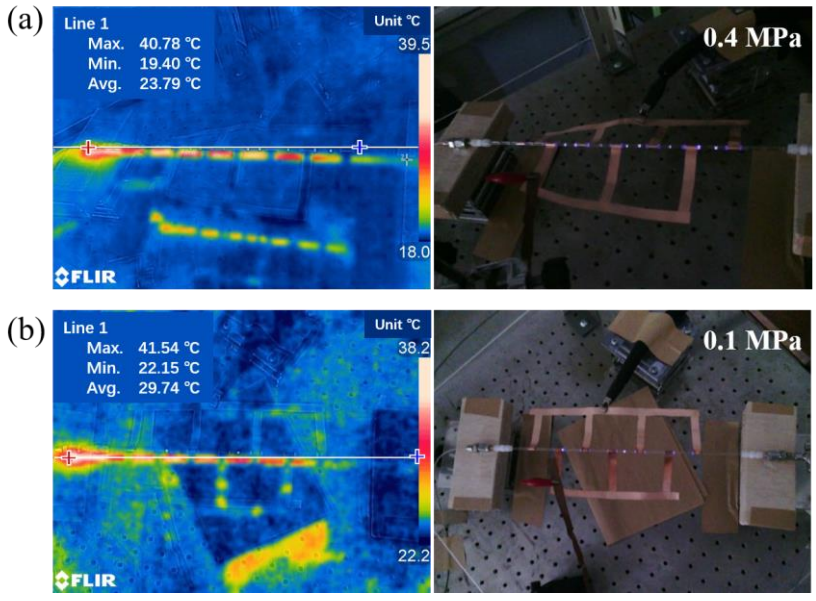

Figure 4.3 Thermal images and visible images of the system under (a) 0.4 MPa and (b) 0.1 MPa

4.3.2 Optical emission spectrum from pulsed discharge plasma

In a gas/liquid environment, various reactive radical species and molecules were generated when plasma was applied into the system. Gas atoms or molecules were ionized by high-energy electrons accelerated in a high local electric field[7], forming initial radicals. Then generated radicals contacted and reacted with water molecules via gas-liquid interface[8], generating more radical species and molecules including hydroxyl radicals and hydrogen radicals[9]. The produced radicals can be involved into various reactions due to their strong reactivity of oxidation or reduction.

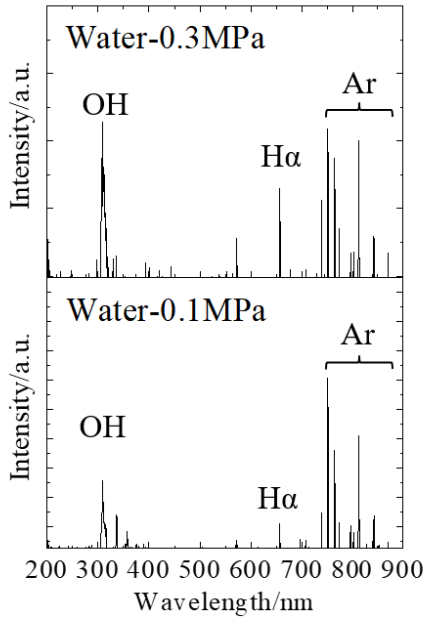

Figure 4.4 Optical emission spectrum from plasma generated in water at 0.1 and 0.3 MPa

Optical emission spectrum from pulsed discharge plasma generated in water at 0.1

and 0.3 MPa were shown as Figure 4.4. Reactive radical species including H· radicals[10], O_2· radicals, and OH· radicals[11] could be observed under each spectrum, indicating the reactive species generated successfully under different pressure after applying the pulsed discharge plasma. The intense emission peak of atomic argon can be observed in the infrared region between 700 and 900 nm[12], originating from the 4p level depopulation through multiple 4p-4s transitions[13-14]. The peak of spectral emission at 656 nm is corresponding to atomic hydrogen, and the intense peak spectral emission at 309 nm is originating from the existence of OH· radicals[15]. As system pressure increased, the types of reactive species generated in the system didn't have significant change, while the relative peak intensities changed. Compared with the peak of atomic argon, peaks intensities of OH· radicals and atomic hydrogen increased, indicating that the relative concentration of OH· and H· radicals increased with system pressure. It might be easier to generate radicals under higher-pressure conditions in this gas/liquid plasma system.

4.3.3 Concentration of total oxidation species

According to the last section, it was known about the generation of OH· and H· radicals in gas/liquid plasma system. OH· radicals continued to combine with each other, generating powerful oxidants including oxygen, hydrogen peroxide, and ozone[16-18]. Concentration of the total oxidation species can be determined by iodimetry, representing the concentration of reactive species generated in the system. The results

are shown in Table 4.1.

Table 4.1. Concentration of total oxidation species under different pressure

Pressure/MPa	c [oxidization species]/mM
0.1	0.12
0.2	0.21
0.3	0.25
0.4	0.29

As results shown, with the system pressure increasing the concentration of total oxidation species increased, being consistent with the results of the optical emission spectra. Therefore, it implied that higher-pressure conditions were beneficial for generation and reaction of radical species in the slug plasma system. Collisions probability between high-energy electrons and agon atoms increased due to increasing pressure and introduced argon gas. More argon atoms were ionized, generating more initial radicals. At the same time, amount of water molecules increased with the increasing density of feed solution, improving the contacts and reactions between initial radicals and water molecules. Hence the concentration of $OH^{\cdot}$ and $H^{\cdot}$ radicals increased, leading to increasing concentration of further generation oxidants. Wu et al.[19] found that generation rate of ozone increased with air flow rate in a dielectric barrier discharge plasma system, because of the promoted collision between electrons and gas molecules. Jiang et al.[20] also reported that more reactive species were generated with gas velocity,

which was due to increasing gas molecules broken down by energetic electrons within the same time span. Concentration of total oxidation species increased with system pressure in this system, demonstrating the potential for application on other reactions.

4.3.4 Input energy calculation

As shown in Paschen's law[21], breakdown voltage required increases when gas pressure continues to increase above a specific value. Plasma was difficult to generate and became unstable as system pressure increased when high voltage of 10 kV was introduced into the slug flow system initially. Hence input voltage was increased to a uniform 11 kV under different system pressure, maintaining a single variable. The voltage and current discharge waveforms were observed by an oscilloscope, which were shown in Figure 4.5 and Figure 4.6. Input energy could be calculated based on the results.

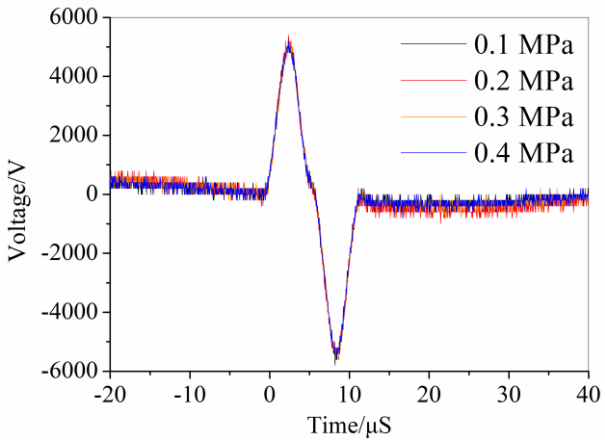

Figure 4.5 Voltage discharge waveforms under different pressure

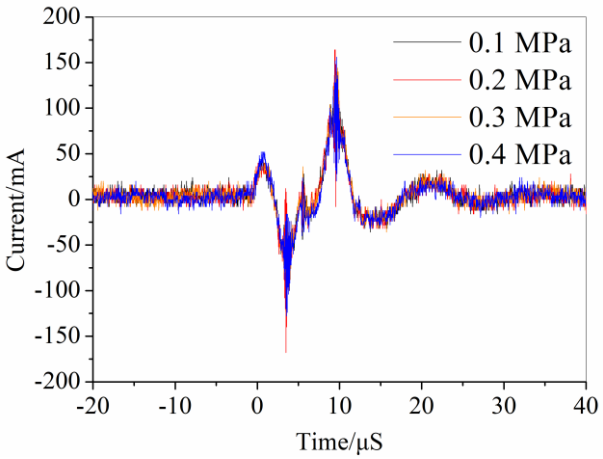

Figure 4.6 Current discharge waveforms under different pressure

As shown in Equation 4-2 to 4-3, pulse energy of discharge plasma is calculated by time integration of the input voltage and current of the plasma reactor. Discharge power is the product of pulse energy and pulse frequency[22]. Calculated results are shown in Table 4.2. As shown in the Table 4.2, as system pressure increased, the input energy was maintained at a stable state without significant changes. In addition, stronger UV radiation was observed during the experiments under pressurized conditions[23], which might increase energy loss.

$$Pulse\ energy = \int V(t) \times I(t)\, dt\ (\mathrm{J/pulse}) \tag{4-2}$$

$$Discharge\ power = Pulse\ energy \times Pulse\ frequency\ (\mathrm{J/s}) \tag{4-3}$$

Table 4.2 Input energy calculation under different pressure

Entry	Pressure/MPa	Power/W	Average/W
1		15.05	
2	0.1	15.31	15.18
3		15.18	
4		15.84	
5	0.2	15.91	16.03
6		16.33	
7		15.63	
8	0.3	15.79	15.73
9		15.75	
10		14.09	
11	0.4	14.53	14.42
12		14.65	

4.4 Conclusion

In this study, the slug flow system with gas/liquid pulsed discharge plasma was successfully implemented under pressurized conditions, providing a novel reaction field. Further insight into the chemical reactivity of this system under high-pressure conditions was studied. The main findings of the study are as follows:

1. Thermal temperature of the slug flow system under pressurized condition was measured. The highest reactor temperature was approximately 40 ℃ under 0.4 MPa, which was acceptably cold.

2. Qualitative and quantitative analyses of reactive species produced in the system under pressurized conditions were studied. Results showed that reactive radical species generated successfully under pressurized conditions after applying pulsed discharge plasma, and the concentration of total oxidation species increased with system pressure.

3. Input energy was calculated based on the voltage and current waveforms of the system. Results showed that it maintained at a steady state under different pressure. And UV radiation became stronger under pressurized conditions, which could increase energy loss.

References

1. Sasaki, K.; Soma, S.; Akashi, H.; ElSabbagh, M.; Ikeda, Y., Electron Temperatures and Electron Densities in Microwave Helium Discharges with Pressures Higher than 0.1 MPa. Wiley Online Library: 2015.
2. Hayashi, Y.; Takada, N.; Kanda, H.; Goto, M., One-step synthesis of water–dispersible carbon nanocapsules by pulsed arc discharge over aqueous solution under pressurized argon. *Research on Chemical Intermediates* **2017,** *43* (7), 4201-4211.
3. Wahyudiono; Watanabe, H.; Machmudah, S.; Kiyan, T.; Sasaki, M.; Akiyama, H.; Goto, M., Pyrrole conversion induced pulse discharge plasma over a water surface under high-pressure argon. *Chemical Engineering and Processing: Process Intensification* **2012,** *61*, 51-57.
4. Lieberman, M. A.; Lichtenberg, A. J., *Principles of plasma discharges and materials processing*. John Wiley & Sons: 2005.
5. Tabares, F. L.; Junkar, I., Cold Plasma Systems and their Application in Surface Treatments for Medicine. *Molecules* **2021,** *26* (7), 1903.
6. Rundle, R.; Baldwin, R., The Configuration of Starch and the Starch—Iodine Complex. I. The Dichroism of Flow of Starch—Iodine Solutions1. *Journal of the American Chemical Society* **1943,** *65* (4), 554-558.
7. Joshi, R. P.; Thagard, S. M., Streamer-Like Electrical Discharges in Water: Part II. Environmental Applications. *Plasma Chemistry and Plasma Processing* **2013,** *33* (1), 17-49.
8. Ognier, S.; Iya-Sou, D.; Fourmond, C.; Cavadias, S., Analysis of mechanisms at the plasma–liquid interface in a gas–liquid discharge reactor used for treatment of polluted water. *Plasma Chemistry and Plasma Processing* **2009,** *29* (4), 261-273.
9. Locke, B. R.; Sato, M.; Sunka, P.; Hoffmann, M. R.; Chang, J. S., Electrohydraulic Discharge and Nonthermal Plasma for Water Treatment. *Industrial & Engineering Chemistry Research* **2006,** *45* (3), 882-905.
10. Potocký, Š.; Saito, N.; Takai, O., Needle electrode erosion in water plasma discharge. *Thin Solid Films* **2009,** *518* (3), 918-923.
11. Huang, F.; Chen, L.; Wang, H.; Yan, Z., Analysis of the degradation mechanism of methylene blue by atmospheric pressure dielectric barrier discharge plasma. *Chemical Engineering Journal* **2010,** *162* (1), 250-256.
12. García, M. C.; Mora, M.; Esquivel, D.; Foster, J. E.; Rodero, A.; Jiménez-Sanchidrián, C.; Romero-Salguero, F. J., Microwave atmospheric pressure plasma jets for wastewater treatment: degradation of methylene blue as a model dye. *Chemosphere* **2017,** *180*, 239-246.
13. Sarani, A.; Nikiforov, A. Y.; Leys, C., Atmospheric pressure plasma jet in Ar and Ar/H 2 O mixtures: Optical emission spectroscopy and temperature measurements. *Physics of Plasmas* **2010,** *17* (6), 063504.
14. Hsieh, K. C.; Wang, H.; Locke, B. R., Analysis of Electrical Discharge Plasma in a Gas‐Liquid Flow Reactor Using Optical Emission Spectroscopy and the Formation

of Hydrogen Peroxide. *Plasma Processes and Polymers* **2016,** *13* (9), 908-917.
15. Mano, K.; Hayashi, Y.; Yamada, M.; Takahashi, S.; Takada, N.; Kanda, H.; Goto, M., Atmospheric-pressure pulsed discharge plasma in capillary slug flow system for dye decomposition. *Chemical Engineering and Processing-Process Intensification* **2019,** *135*, 133-140.
16. Chu, P. K.; Lu, X., Low temperature plasma technology: methods and applications. CRC Press: 2013.
17. Lu, N.; Li, J.; Wu, Y.; Masayuki, S., Treatment of Dye Wastewater by Using a Hybrid Gas/Liquid Pulsed Discharge Plasma Reactor. *Plasma Science and Technology* **2012,** *14* (2), 162-166.
18. Sun, B.; Aye, N. N.; Gao, Z.; Lv, D.; Zhu, X.; Sato, M., Characteristics of gas-liquid pulsed discharge plasma reactor and dye decoloration efficiency. *Journal of Environmental Sciences* **2012,** *24* (5), 840-845.
19. Wu, L.; Xie, Q.; Lv, Y.; Wu, Z.; Liang, X.; Lu, M.; Nie, Y., Degradation of Methylene Blue via Dielectric Barrier Discharge Plasma Treatment. *Water* **2019,** *11* (9), 1818.
20. Jiang, B.; Zheng, J.; Liu, Q.; Wu, M., Degradation of azo dye using non-thermal plasma advanced oxidation process in a circulatory airtight reactor system. *Chemical Engineering Journal* **2012,** *204-206*, 32-39.
21. Babich, L.; Loĭko, T. V., Generalized Paschen's Law for Overvoltage Conditions. *IEEE Transactions on Plasma Science* **2016,** *44* (12), 3243-3248.
22. Okumoto, M.; Mizuno, A., Conversion of methane for higher hydrocarbon fuel synthesis using pulsed discharge plasma method. *Catalysis today* **2001,** *71* (1-2), 211-217.
23. Diono, W.; Machmudah, S.; Kanda, H.; Zhao, Y.; Goto, M., Pulsed Discharge Plasma in High-Pressure Environment for Water Pollutant Degradation and Nanoparticle Synthesis. *Plasma* **2021,** *4* (2), 309-331.

Chapter 5. Decomposition of methylene blue using pulsed discharge plasma in the slug flow reactor under pressurized argon

5.1 Introduction

5.1.1 Methylene blue

Methylene blue (MB) is a pollutant commonly present in textile wastewater. When discharged as industrial effluent, it would make the water inhibitory for aquatic life, causing severe environmental and health problems[1]. And it has a complex and stable structure due to the existence of chromophore and auxochrome[2], as shown in Figure 5.1. Until now, several methods have been reported on the removal of MB, including adsorption[3], biodegradation[4], ozonation[5], photocatalytic degradation[6]. Lkhlaq et al.[7] proposed the catalytic ozonation process to decompose MB in wastewater, which is found effective. Ahmad et al.[8] reported the degradation method of MB via photocatalysis using activated carbon, in which free radicals and superoxide played an important role.

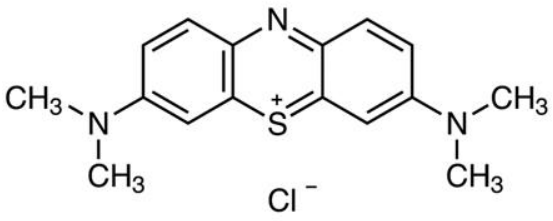

Figure 5.1 Structure of methylene blue[9]

5.1.2 Decomposition mechanism of methylene blue

During the processes of chemical methods, MB is degraded mainly by oxidation reactions to break the rings into small molecular compounds. Wang et al.[10] reported the pathways of MB degradation by Fenton process, oxidization of MB with hydroxy radicals generated by catalytic decomposition on hydrogen peroxide. Houas et al.[6] also reported that during the photocatalytic MB degradation pathway, the degradation intermediates originated from opening initially the central aromatic ring by photocatalytic oxidation with hydroxy radicals.

Various chemically active species are produced in the systems of gas/liquid discharge plasma. As an advanced oxidation process, cold plasma technologies showed specific advantages in situ generation of strong oxidants and absence of by-products[11]. Huang et al.[12] have reported the degradation process of MB using the dielectric barrier discharge plasma. Ozone, hydroxyl radicals and other active species are generated, breaking the N–CH_3 bond and oxidizing –CH_3 into HCHO or HCOOH. Then C–S and C–N bonds in the remaining structure are destroyed to generate phenyl thiophene and other molecular structures, being oxidized into inorganic ions finally.

5.1.3 Motivation and purpose of this work

In this study, the slug flow system using pulsed discharge plasma is applied on decomposition of MB under atmospheric and pressurized argon, respectively. MB is degraded using chemical methods mainly because of the oxidation reactions to break

the ring into small molecular compounds. According to the results in Chapter 4, the concentration of total oxidation species increased with the increasing system pressure. Hence, the ability of the system on dye decomposition is expected to be improved under pressurized conditions. The decomposition rates of MB under different system pressure are calculated by the results of UV-vis, and the effect of system pressure on the decomposition of MB is also investigated.

5.2 Experimental procedure

5.2.1 Materials

Methylene blue ($C_{16}H_{18}N_3SCl$) (Product No. 133-06962), sodium chloride (NaCl, 99.5%) (Product No. 191-01665) and distilled water (Product No. 049-16787) were purchased from Wako Pure Chemical Industries, Ltd., Osaka, Japan. Argon (purity > 99.99%) was purchased from Sogo Kariya Sanso, Inc., Nagoya, Japan. All the chemicals used in this study were used as received without further purification.

5.2.2 Experimental methods

Experimental methods using in this Chapter is similar with that in Chapter 3.3.2. MB solution of 15mg/L was used as the feed solution, and NaCl was added to provided conductivity to approximately 1 mS/cm for plasma generation.

5.2.3 Analysis methods

The use of UV-vis is same with Chapter 2.2.3. The use and analysis of optical emission spectra are same with Chapter 3.2.3.

5.2.4 Dye decomposition rate of MB

Feed solution and products after plasma treatments were characterized using UV-vis, showing a characteristic peak of MB at approximately 664 nm[13-14]. Intensity of the peak is directly proportional to the concentration of MB. Through the ratio of peaks intensities of feed solution and the products, decomposition rates could be calculated as Equation 5-1.

$$Decomposition\ rate = \left[1 - \frac{A_p}{A_f}\right] \times 100\% \quad (5\text{-}1)$$

where A_p and A_f are peaks intensities of the products under different pressure and feed solution at 664 nm, respectively.

5.3 Results and discussion

5.3.1 Optical emission spectra from pulsed discharge plasma

Decomposition of MB is mainly due to the ring breaking reactions to generating small molecular compound[15]. Reactive species with strong oxidative ability were dominant on decomposition of MB. Hence the types of reactive species generated by pressurized plasma in MB were analyzed. Optical emission spectra were shown in Figure 5.2.

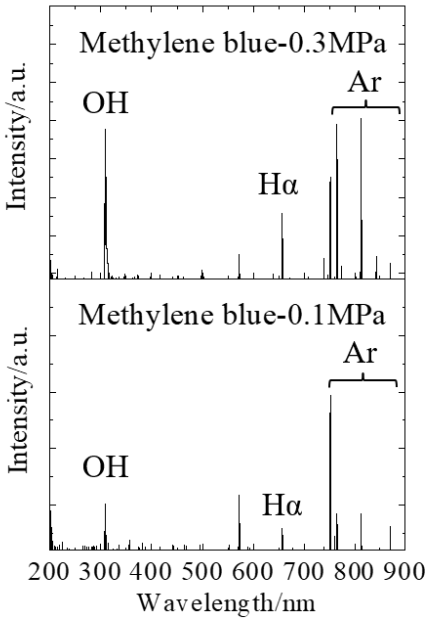

Figure 5.2 Optical emission spectra from plasma generated in MB at 0.1 and 0.3 MPa

As Figure 5.2 shown, the spectral emission peaks of OH· radicals, atomic hydrogen, and atomic argon could be observed in the spectra, indicating the successful generation of reactive species in the MB solution. As system pressure increased, types of reactive species had not significant change while the relative concentration of OH· radicals and H· radicals increased. The results were similar with that in water (Chapter 4.3.2). Hence, further analysis of this section was omitted.

5.3.2 Effect of electrodes number on dye decomposition rates

At first, 3 electrodes including 1 high-voltage electrode and 2 ground electrodes

were arranged on the slug flow reactor, as shown in Figure 5.3 a. Decomposition rates of MB under different system pressure were calculated and shown in Table 5.1. According to the section 3.3.3, it was found that concentration of reactive species generated by plasma increased with electrodes number, leading to the increase on the concentration of products. Therefore, electrodes number was increased to 7, including 4 high-voltage electrodes and 3 ground ones, as shown in Figure 5.3 b. And the residence time of plasma-state bubbles increased from 6 s to 20 s approximately. The UV-vis spectra of feed solution and products after plasma treatments under different pressure were shown in Figure 5.4. Decomposition rates of MB with 7 electrodes were also calculated and shown in Table 5.2. Results shown a significant increase on decomposition rate of MB when using 7 electrodes, consistent with the results in section 3.3.3.

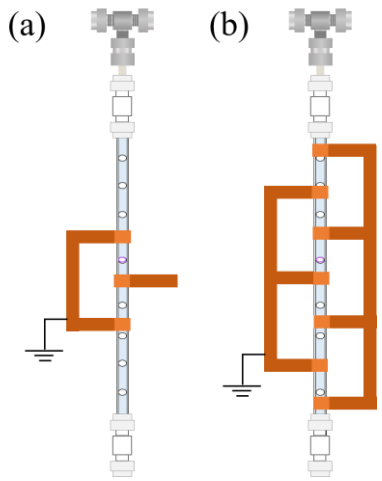

Figure 5.3 Slug flow reactors with (a) three (two ground and one high-voltage) electrodes; (b) seven (three ground and four high-voltage) electrodes

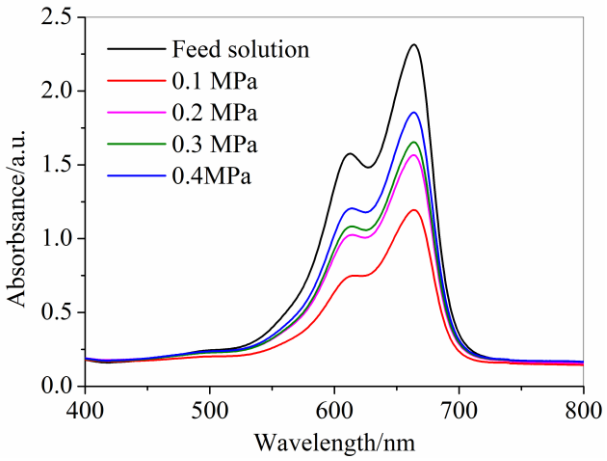

Figure 5.4 UV-vis spectra of solution and products under different pressure with 7 electrodes

Table 5.1 Decomposition rate of MB with 3 electrodes

Pressure/MPa	Electrodes number	Decomposition rate/ %
0.1	3	20.25
0.2	3	13.72
0.3	3	9.95

Table 5.2 Decomposition rate of MB with 7 electrodes

Pressure/MPa	Electrodes number	Decomposition rate/ %
0.1	7	48.42
0.2	7	32.36
0.3	7	28.57
0.4	7	19.89

According to both Table 5.1 and Table 5.2, it was observed that decomposition rate of MB decreased with system pressure increasing. But as the results in Chapter 4.3.3

shown, the concentration of total oxidation species increased with system pressure, and reactive oxidation species generated in the system were dominant for decomposition rate of MB. This was inconsistent with the decrease of decomposition rates. Hence, the reasons would be attempted to be explained from the energy perspective in the next section.

5.3.3 Effect of system pressure on energy efficiency

Energy efficiency for the decomposition is evaluated by calculating the consumed input energy per degradation of unit MB[16]. In this study, it was calculated by combining the results of input power (section 4.3.4) with decomposition rates of MB when using 7 electrodes (section 5.3.2), as shown in Equation 5-2. The results were shown in Table 5.3.

$$Energy\ efficiency = \frac{C_0\ (\mathrm{g/L}) \times Q\ (\mathrm{L/h}) \times Decomposition\ rate\ (\%) \times \frac{1}{100}}{Discharge\ power\ (\mathrm{kW})} \quad (5\text{-}2)$$

where C_0 and Q are the concentration and flow rate of MB, respectively.

Table 5.3 Energy and energy efficiency under different system pressure

Pressure/MPa	Power/W	Energy efficiency/g·kWh^{-1}
0.1	15.18	0.044
0.2	16.03	0.029
0.3	15.73	0.026
0.4	14.42	0.018

As shown in the Table 5.3, energy efficiency of MB decomposition in the system with pulsed discharge plasma decreased with system pressure increasing. On theory, the collision between high-energy electrons and gas atoms or molecules improved due to the increase on system pressure and distribution density of gas. Excitation or ionization of atoms or molecules caused by inelastic collisions was promoted, resulting in an increase on energy loss[17]. Also, physical effects including UV radiation, shock wave generation, and strong electrical field happened when high-voltage plasma was introduced into a gas/liquid medium[18-20]. As above mentioned, the emission intensity of the cold plasma increased under pressurized conditions[21], which might also increase the energy loss. In addition, direct photooxidation of dye in the water was very limited because of the great absorption of UV radiation in water[22], leading to the result that enhanced UV radiation also had no significant effect on decomposition of MB.

On basis of the similar total input energy, the energy loss increased with system pressure, leading to a decrease on energy provided for decomposition of MB. Feng et al.[23] reported that the degradation efficiency of diuron increased as input power intensity. Wang et al.[24] also found that removal rate of acid orange increased with energy acting to degrade organic compounds in water increasing. Therefore, the reason for the decrease of MB decomposition rate may be due to the limited energy provided under high-pressure conditions.

5.4 Conclusion

In this study, the slug flow system using gas/liquid discharge plasma was applied for the decomposition of MB under pressurized conditions. Dye decomposition rate and energy efficiency under different pressure were calculated. Results showed that the types of reactive species generated in MB were similar with that in water. As system pressure increased, the types of reactive species didn't have significant change while the relative concentration of $OH^{\cdot}$ radicals and $H^{\cdot}$ radicals increased. With system pressure increasing, dye decomposition rate of MB and energy efficiency decreased, which could be explained by the decrease on energy available for dye decomposition because of the increase on energy loss under higher-pressure conditions and steady input energy.

References

1. He, P. Y.; Zhang, Y. J.; Chen, H.; Liu, L. C., Development of an eco-efficient CaMoO4/electroconductive geopolymer composite for recycling silicomanganese slag and degradation of dye wastewater. *Journal of Cleaner Production* **2019,** *208*, 1476-1487.
2. Tichonovas, M.; Krugly, E.; Racys, V.; Hippler, R.; Kauneliene, V.; Stasiulaitiene, I.; Martuzevicius, D., Degradation of various textile dyes as wastewater pollutants under dielectric barrier discharge plasma treatment. *Chemical Engineering Journal* **2013,** *229*, 9-19.
3. Sharma, K.; Vyas, R. K.; Dalai, A. K., Thermodynamic and Kinetic Studies of Methylene Blue Degradation Using Reactive Adsorption and Its Comparison with Adsorption. *Journal of Chemical & Engineering Data* **2017,** *62* (11), 3651-3662.
4. Eslami, H.; Sedighi Khavidak, S.; Salehi, F.; Khosravi, R.; Fallahzadeh, R. A.; Peirovi, R.; Sadeghi, S., Biodegradation of methylene blue from aqueous solution by bacteria isolated from contaminated soil. *Journal of Advances in Environmental Health Research* **2017,** *5* (1), 10-15.
5. Zhang, J.; Lee, K.-H.; Cui, L.; Jeong, T.-s., Degradation of methylene blue in aqueous solution by ozone-based processes. *Journal of Industrial and Engineering Chemistry* **2009,** *15* (2), 185-189.
6. Houas, A.; Lachheb, H.; Ksibi, M.; Elaloui, E.; Guillard, C.; Herrmann, J.-M., Photocatalytic degradation pathway of methylene blue in water. *Applied Catalysis B: Environmental* **2001,** *31* (2), 145-157.
7. Ikhlaq, A.; Munir, H. M. S.; Khan, A.; Javed, F.; Joya, K. S., Comparative study of catalytic ozonation and Fenton-like processes using iron-loaded rice husk ash as catalyst for the removal of methylene blue in wastewater. *Ozone: Science & Engineering* **2019,** *41* (3), 250-260.
8. Ahmad, A.; Jini, D.; Aravind, M.; Parvathiraja, C.; Ali, R.; Kiyani, M. Z.; Alothman, A., A novel study on synthesis of egg shell based activated carbon for degradation of methylene blue via photocatalysis. *Arabian Journal of Chemistry* **2020,** *13* (12), 8717-8722.
9. Faical, M.; Atmani, R.; Talbi, M.; Amardo, N., Adsorption of methylene blue in solution on activated carbon based of banana peels residue. *International Journal of Scientific and Engineering Research* **2018,** *9*, 617-622.
10. Wang, Q.; Tian, S.; Ning, P., Degradation Mechanism of Methylene Blue in a Heterogeneous Fenton-like Reaction Catalyzed by Ferrocene. *Industrial & Engineering Chemistry Research* **2014,** *53* (2), 643-649.
11. Oturan, M., An ecologically effective water treatment technique using electrochemically generated hydroxyl radicals for in situ destruction of organic pollutants: application to herbicide 2, 4-D. *Journal of Applied Electrochemistry* **2000,** *30* (4), 475-482.
12. Huang, F.; Chen, L.; Wang, H.; Yan, Z., Analysis of the degradation mechanism of methylene blue by atmospheric pressure dielectric barrier discharge plasma. *Chemical Engineering Journal* **2010,** *162* (1), 250-256.

13. Chang, H.; Su, C.; Lo, C.-H.; Chen, L.-C.; Tsung, T.-T.; Jwo, C.-S., Photodecomposition and surface adsorption of methylene blue on TiO2 nanofluid prepared by ASNSS. *Materials transactions* **2004,** *45* (12), 3334-3337.
14. Jiao, Q.; Liu, Q., Characterization of the interaction between methylene blue and glycosaminoglycans. *Spectrochimica Acta Part A: Molecular and Biomolecular Spectroscopy* **1999,** *55* (7-8), 1667-1673.
15. Corella Puertas, E.; Peyot, M.-L.; Pineda, M.; Volk, K.; Coulombe, S.; Yargeau, V., Degradation of diatrizoate in a pin-to-liquid plasma reactor, its transformation products and their residual toxicity. *Science of The Total Environment* **2021,** *782*, 146895.
16. Sun, Y.; Cheng, S.; Lin, Z.; Yang, J.; Li, C.; Gu, R., Combination of plasma oxidation process with microbial fuel cell for mineralizing methylene blue with high energy efficiency. *Journal of Hazardous Materials* **2020,** *384*, 121307.
17. Atomic Collisions. In Principles of Plasma Discharges and Materials Processing, 2005; pp 43-85.
18. Locke, B.; Sato, M.; Sunka, P.; Hoffmann, M.; Chang, J.-S., Electrohydraulic discharge and nonthermal plasma for water treatment. *Industrial & engineering chemistry research* **2006,** *45* (3), 882-905.
19. Abramov, V. O.; Abramova, A. V.; Cravotto, G.; Nikonov, R. V.; Fedulov, I. S.; Ivanov, V. K., Flow-mode water treatment under simultaneous hydrodynamic cavitation and plasma. *Ultrasonics Sonochemistry* **2021,** *70*, 105323.
20. Sun, B.; Xin, Y.; Zhu, X.; Gao, Z.; Yan, Z.; Ohshima, T., Effects of shock waves, ultraviolet light, and electric fields from pulsed discharges in water on inactivation of Escherichia coli. *Bioelectrochemistry* **2018,** *120*, 112-119.
21. Diono, W.; Machmudah, S.; Kanda, H.; Zhao, Y.; Goto, M., Pulsed Discharge Plasma in High-Pressure Environment for Water Pollutant Degradation and Nanoparticle Synthesis. *Plasma* **2021,** *4* (2), 309-331.
22. Sugiarto, A. T.; Ito, S.; Ohshima, T.; Sato, M.; Skalny, J. D., Oxidative decoloration of dyes by pulsed discharge plasma in water. *Journal of Electrostatics* **2003,** *58* (1), 135-145.
23. Feng, J.; Zheng, Z.; Luan, J.; Li, K.; Wang, L.; Feng, J., Gas–liquid hybrid discharge-induced degradation of diuron in aqueous solution. *Journal of Hazardous Materials* **2009,** *164* (2), 838-846.
24. Wang, H.; Li, J.; Quan, X., Decoloration of azo dye by a multi-needle-to-plate high-voltage pulsed corona discharge system in water. *Journal of Electrostatics* **2006,** *64* (6), 416-421.

Chapter 6. Conclusion

This study focused on the slug flow system using pulsed discharge plasma for synthesis of metal oxide nanoparticles and dye decomposition. Compared with traditional methods to produce gas/liquid plasma, the slug flow system provided a continuous and stable reaction field, beneficial for generating stable plasma and synthesizing nanoparticles. During the process, toxic solvents and ligands were not required, decreasing the operating cost and environmental stress. And this system was first implemented under pressurized argon. The insight of chemical properties on the system was investigated under pressurized conditions.

In Chapter 2, cerium nitrate, magnesium chloride, and zinc chloride aqueous solutions of 1 mmol/L were used as feed solution to synthesize corresponding metal oxide nanoparticles in the system under atmospheric conditions. The products were characterized by several analysis methods, including TEM, EDS, HRTEM, and UV-vis. Results showed that cerium dioxide, magnesium oxide, and zinc oxide nanoparticles were successfully synthesized by the slug flow system using pulsed discharge plasma.

In Chapter 3, cerium dioxide nanoparticles were selected as the target product to investigated the synthesis mechanism and effect of different experimental factors. Besides the straight capillary glass tube, a circular capillary glass tube coil was also used as the slug flow reactor. Results showed that when using circular capillary glass tube coil as the reactor, residence time was prolonged and electrodes number was increased, leading an increase on the concentration of cerium dioxide nanoparticles. The mean size of cerium dioxide nanoparticles also increased from 3.4 nm to 6.3 nm.

Starch was added into feed solution as a stabilizer to cap cerium ions to separate adequately the nucleation and growth process, preventing nanoparticles aggregation. When tetravalent cerium ions were used as the feed solution, cerium trioxide nanoparticles were also generated, which might because a part of tetravalent cerium ions were reduced by the hydrogen radicals generated by gas/liquid plasma.

In Chapter 4, the slug flow system using gas/liquid discharge plasma was first utilized under pressurized conditions. The thermal temperature of reactor under pressurized argon was measured, being acceptably cold, a little higher than room temperature. Calculated input energy was maintained constant under different system pressure. Reactive species generated in the gas/liquid discharge plasma system were qualitatively and quantitatively analyzed to investigate the chemical reactivity. Results showed that the types of reactive species have no significant change under pressurized argon. The concentration of total oxidation species increased with increasing system pressure.

In Chapter 5, the system was applied on the dye decomposition of methylene blue under pressurized conditions. The dye decomposition rates were calculated and effect of experimental factors was studied. Results showed that dye decomposition rates increased greatly with the increasing electrodes number. But as system pressure increased, dye decomposition rates decreased. This might be due to the constant input energy and increasing energy loss under pressurized conditions, resulting in a decrease on the energy available for dye decomposition.

Achievement

List of publications

[1] Zhu, W.; Lin, Y.; Zhu, L.; Wahyudiono; Honda, M.; Kanda, H.; Goto, M., Synthesis of cerium dioxide nanoparticles by gas/liquid pulsed discharge plasma in a slug flow reactor. ACS omega 2021, 6 (32): 20966-20974.

[2] Zhu, W.; Wahyudiono.; Kanda, H; Goto, M., Gas/liquid pulsed discharge plasma in a slug flow reactor under pressurized argon for dye decomposition. ACS omega 2022, 7 (15): 12993-12999.

[3] Zhu, L.; Zhu, W.; Hu, X.; Lin, Y.; Machmudah, S.; Wahyudiono; Kanda, H.; Goto, M., PVP/highly dispersed AgNPs nanofibers using ultrasonic-assisted electrospinning. Polymers 2022, 14(3): 599.

[4] Lin, Y.; Zhu, W.; Gou, R.; Kita, H.; Hu, X.; Zhu, L.; Wahyudiono; Kanda, H.; Goto, M., Synthesis of carbon-encapsulated metal-based nanoparticles by gas/liquid interfacial plasma under high pressure. Journal of environmental chemical engineering 2022, 10(3): 107771

List of presentations

[1] Zhu, W., Wahyudiono, Kanda, H., Goto, M., “Synthesis of cerium oxide nanoparticles by non-thermal plasma in slug flow reactor system”, 81st JSAP Autumn Conference, Virtual, Oral, September 8-11, 2020

[2] Zhu, W., Wahyudiono, Kanda, H., Goto, M., “Synthesis of cerium oxide nanoparticles by atmospheric-pressure pulsed discharge plasma”, 73rd Gaseous Electronics Conference, Virtual, Oral, October 5-9, 2020

[3] Zhu, W., Wahyudiono, Kanda, H., Goto, M., “Synthesis of cerium dioxide nanoparticles by gas/liquid pulsed discharge plasma in a slug flow reactor”, 2021 IEEE International Conference on Plasma Science, Virtual, Poster, September 12-16, 2021

[4] Zhu, W., Wahyudiono, Kanda, H., Goto, M., “Dye decomposition by pulsed discharge plasma flow reactor under a pressurized condition”, The 82nd JSAP Autumn Meeting, Virtual, Poster, September 21-23, 2021

[5] Zhu, W., Wahyudiono, Kanda, H., Takami, S., Goto, M., “Gas/liquid pulsed discharge plasma in a slug flow reactor under pressurized conditions for dye decomposition", 2022 IEEE International Conference on Plasma Science, Virtual, Poster, May 22-26, 2022

Acknowledgement

Firstly, I would like to express my deepest gratitude to Prof. Motonobu Goto and Dr. Hideki Kanda for their continuous support and teaching. I feel particularly fortunate to have joined in Goto laboratory. Goto sensei has been giving me warm and patient support, giving me efficient guidance on my research topic and preparation of the manuscripts. He also encouraged me to attend the academic conferences to improve myself. Kanda sensei always carefully helped me revise the manuscripts, seminar slides, posters, and doctoral thesis. His seriousness also encouraged me. It would be difficult for me to successfully complete my PhD project without their help.

I would also like to express my sincere thanks to Dr. Wahyudiono for his all help on my research and manuscripts. Every time I had questions in the experiments and manuscripts, Wahyu san had the ability to help me solve them. I also learned a lot from the discussions with him.

Next, I would like to sincerely thank Prof. Seiichi Takami for his all help on my PhD graduation process. He carefully helped me arrange the pre-defense and defense, and always reminded me on the schedule. And I am also grateful to the Prof. Koyo Norinaga and Prof. Hirotaka Toyoda, giving me meaningful comments on my thesis and presentation.

I would also express my gratitude to office assistant Rika Osawa san, Yuki Inagaki san, and Akira Ishibashi san. They helped me a lot on the affairs and life in Nagoya University. And I also thank all members in Goto laboratory and Kanda group for their help and support, giving me more tolerance because of my status as a foreigner.

In addition, I would also like to express my thanks for technical support of High Voltage Electron Microscope Laboratory, Research Facility for Advanced Science and Technology, and Engineering Research Committee in Nagoya University.

Finally, my hearty thanks go to my parents and friends for their support and encouragement all through my study life. Thanks to everyone who helped me during my life in Japan. I sincerely wish everyone peace and happiness.